PHYSICAL REVIEW D **76,** 104015 (2007)

Binary black-hole evolutions of excision and puncture data

Ulrich Sperhake*

Theoretisch-Physikalisches Institut, Friedrich-Schiller-Universität Max-Wien-Platz 1, 07743 Jena, Germany

(Received 18 June 2006; revised manuscript received 1 July 2007; published 9 November 2007)

We present a new numerical code developed for the evolution of binary black-hole spacetimes using different initial data and evolution techniques. The code is demonstrated to produce state-of-the-art simulations of orbiting and inspiralling black-hole binaries with convergent waveforms. We also present the first detailed study of the dependence of gravitational waveforms resulting from three-dimensional evolutions of different types of initial data. For this purpose we compare the waveforms generated by head-on collisions of superposed Kerr-Schild, Misner, and Brill-Lindquist data over a wide range of initial separations.

DOI: 10.1103/PhysRevD.76.104015 PACS numbers: 04.25.Dm

I. INTRODUCTION

In the course of the last two years, the research area of gravitational wave physics has entered a very exciting era. On the experimental side, the first generation of ground-based gravitational wave detectors, LIGO, GEO600, TAMA300, and VIRGO, are performing observation runs at and even beyond design sensitivity [1–5]. At the same time, the simulation of the most promising sources of gravitational waves, the inspiral of compact binary systems, has made enormous progress. While approximate studies based on the post-Newtonian approach have been able for some time to accurately simulate the earlier stages of inspiralling binary systems [6–11], recent developments in numerical relativity have made possible the simulation of the highly relativistic final stages of the inspiral and merger of compact binaries in the framework of fully nonlinear general relativity.

For a long time such simulations have been troubled by stability problems which caused evolutions to terminate after times relatively short compared with the dynamic time scales of the problems under investigation. It is becoming increasingly clear now, however, that these problems have been successfully overcome by a combination of modified formulations of the Einstein equations [12–15], suitable gauge conditions (see e.g. [16–19]) and improved techniques for the treatment of the singularities inherent to black-hole spacetimes.

Using such modern techniques, Brügmann *et al.* [17] obtained the first simulation of a complete orbit of a black-hole binary in the framework of the Baumgarte-Shapiro-Shibata-Nakamura (BSSN) formulation [12,13], using puncture data [20] and corotating coordinates. More recently, their results have been confirmed by an improved study [21]. The first waveforms generated in the inspiral and coalescence of black holes have been presented by Pretorius [22,23] who uses a generalized harmonic formulation of the Einstein equations combined with special numerical techniques such as black-hole excision, spatial compactification, and implicit finite differencing. The latest development, simultaneously discovered by Campanelli *et al.* and Baker *et al.* [18,19,24,25], is based on the evolution of black-hole data of puncture type using special gauge conditions accommodating the motion of the punctures across the computational domain. For this reason these simulations are commonly referred to as *moving punctures*. More recently, this technique has facilitated the investigation of various aspects of the binary black-hole coalescence, such as the radiation of linear momentum by systems of unequal masses and/or spins [26–34], the impact on the waveforms and merger dynamics of nonvanishing spins [35,36] and analysis of the waveforms in the framework of post-Newtonian inspiral and black-hole ring-down [37–42].

As in the case of black holes, simulations lasting for several orbits have also been obtained for neutron star binaries by several groups [43–46]. In more recent developments the focus is switching to the refinement of the matter models by including, for example, magneto-hydrodynamic effects (see e.g. [47]). In our work, however, we focus on black-hole systems, and will therefore exclusively study vacuum spacetimes.

In spite of the dramatic progress in numerical simulations of black-hole binaries, there remain important questions to be answered, in particular, with regard to the use of the resulting waveforms in the ongoing effort to detect and physically interpret gravitational-wave signals. In particular, it will be important to establish the accuracy of the numerically calculated waveforms and the consistency of these results with regard to the use of different types of binary-black-hole initial data and the evolution techniques used in the codes. First steps in this direction have been undertaken with regard to the use of evolution techniques and separation parameters of a given initial-data type. In Ref. [48], the impact of black-hole excision was studied in the case of head-on collisions of Brill-Lindquist data. The results with and without excision yielded good agreement in that study. A comparison between plunge waveforms obtained from moving-puncture evolutions with those resulting from Lazarus calculations [49] has been presented

*Ulrich.Sperhake@uni-jena.de

in Ref. [19]. Furthermore, the waveforms resulting from inspiralling black holes of puncture type starting from different separations have been found to show excellent agreement in Refs. [27,35]. A comparison of waveforms obtained from evolving conceptually different types of initial data has been presented in [50]. This study is inhibited, however, by the difficulties in starting the simulations from comparable initial configurations as is demonstrated by the nonvanishing spin in one of the two data sets considered in this work.

The purpose of this paper is twofold. First, we present a new numerical code which has been designed to accommodate different types of initial data, formulations of the Einstein equations as well as singularity treatment. We demonstrate that the code is capable of producing state-of-the-art simulations of inspiralling black-hole binaries and extract convergent waveforms. Second, we use the code to further progress in the comparison of different initial configurations by comparing black-hole head-on collisions obtained from different types of initial data and using different evolution techniques. Specifically, we compare the results obtained from superposed Kerr-Schild data evolved in the framework of black-hole excision and algebraic gauge conditions with those obtained from evolving Brill-Lindquist as well as Misner data in the framework of the moving-puncture method.

This paper is structured as follows. We begin with a detailed presentation of the code in Sec. II. Next, we benchmark the code in Sec. III by simulating the inspiral and merger of an orbiting black-hole binary comparable to those studied in the recent literature. The comparison of head-on collisions obtained with Brill-Lindquist, Misner, and Kerr-Schild data is given in Sec. IV and we conclude with a discussion of our findings in Sec. V. Details on the exact version of the BSSN equations used for this work, the analytic solution of a boosted black hole in Kerr-Schild coordinates, extraction of gravitational waves, and the performance of the code are presented in Appendixes A, B, C, and D. Throughout this work we set $G = c = 1$ and use Greek indices for spacetime components $0 \ldots 3$ and Latin indices for spatial components $1 \ldots 3$.

II. COMPUTATIONAL FRAMEWORK

The simulations presented in this work have been obtained with the newly developed LEAN code. This code has been inspired partly by the MAYA[1] code [51–53], and partly by the most recent developments in the simulation of black-hole data of puncture type [24,25]. It is based on the CACTUS computational toolkit [54], used for parallelization and data input/output. Mesh refinement is provided by CARPET [55,56], puncture initial data by the TWOPUNCTURES thorn [57], and horizon finding by AHFINDERDIRECT [58,59]. The code achieves dynamic mesh refinement by steering in accordance with the black-hole motion the regridding option inherent to the CARPET package. While the LEAN code has been inspired by MAYA, it has been written entirely from scratch and various new features have been added. These are fourth-order discretization of the spatial derivatives, the evolution of the BSSN equations using the χ version (see below), additional gauge conditions, time integration using the fourth-order Runge-Kutta (RK) scheme, dynamic mesh refinement that allows for multiple refinement components to follow the black-hole motion and merge into single components and additional initial-data options including puncture data using the TWOPUNCTURE thorn [57] and Misner data. Furthermore, the different organization of the code has led to about 5 times faster evolutions and a reduction by about a third in memory requirements compared with MAYA for a given configuration. Details on the code's performance for the orbital simulations and head-on collisions are provided in Appendix D. The key feature of the code for the comparison presented below is the incorporation in the framework of mesh refinement of both dynamic black-hole excision and the moving-puncture technique used with enormous success in evolutions of conformally flat initial data. These features as well as other aspects of the LEAN code are described in more detail in the remainder of this section.

A. Formulation of the Einstein equations

Most of the numerical work in three spatial dimensions has been performed inside the framework of the canonical "3 + 1" spacetime decomposition of Arnowitt, Deser, and Misner (ADM) [60] (see also [61] for a detailed discussion). In the notation of [61], the geometry is described in terms of the three-dimensional metric γ_{ij} and the extrinsic curvature K_{ij}, as well as four gauge functions α and β^i which represent the coordinate freedom of general relativity. The Einstein field equations result in six evolution equations each for γ_{ij} and K_{ij} as well as four constraint equations, namely, the Hamiltonian and momentum constraints. These equations are commonly referred to as the ADM equations.

While these equations have been at the heart of most numerical codes for a long time, the ensuing stability problems have led to the use of various alternative formulations of the Einstein equations, most of them modifications of the ADM equations. The most popular and successful of these modified schemes is now known as the BSSN system [12,13] and has been implemented in the LEAN code. While the code also allows evolutions using the Nagy-Ortiz-Reula (NOR) [62] or the generalized harmonic formulation [14,15], we have not yet managed to achieve long-term stable simulations using these systems. Therefore, all simulations presented in this work have been obtained with the BSSN system.

[1]Throughout this work with the MAYA code we refer to the version used in Ref. [51] which is not to be confused with the new code of the same name described in Ref. [26].

The BSSN formulation results from applying the following modifications to the original ADM equations: First, a split of the extrinsic curvature into a trace-free part A_{ij} and the trace K; second, a conformal rescaling of the three-metric and the extrinsic curvature; and, third, the introduction of contracted Christoffel symbols as separate variables $\tilde{\Gamma}^i$. One thus arrives at a description of the spacetime in terms of the variables

$$\phi = \frac{1}{12}\ln\gamma, \qquad \tilde{\gamma}_{ij} = e^{-4\phi}\gamma_{ij}, \qquad K = \gamma^{ij}K_{ij},$$
$$\tilde{A}_{ij} = e^{-4\phi}\left(K_{ij} - \frac{1}{3}\gamma_{ij}K\right), \qquad \tilde{\Gamma}^i = \tilde{\gamma}^{mn}\tilde{\Gamma}^i_{mn}, \tag{1}$$

as well as the gauge functions α and β^i. Here, γ denotes $\det\gamma_{ij}$ and the definition of ϕ implies that $\tilde{\gamma} = \det\tilde{\gamma}_{ij} = 1$. Alternatively to this choice of variables the LEAN code also allows for evolutions using the variable

$$\chi = e^{-4\phi} \tag{2}$$

as introduced in Ref. [24]. The complete evolution equations for both sets of variables are listed in Appendix A. We refer to the two resulting systems given by Eqs. (A1)–(A5) and Eqs. (A1), (A4), and (A6)–(A8) as the ϕ and the χ version of the BSSN equations, respectively, in the remainder of this work.

In addition to evolving the BSSN variables according to either of these systems, we enforce after each update of the variables the condition $\tilde{A}^i{}_i = 0$, which is a consequence of the definition of $\tilde{A}_{ij}$ in Eq. (1). We find this step to be crucial for the stability of our simulations. Other modifications to the BSSN equations have been suggested in the literature (see e.g. [63]). We have experimented with several of these, but not observed any further improvements of the performance of the code. In particular, we do not find it necessary to enforce the condition $\det\tilde{\gamma}_{ij} = 1$ or to replace the variable $\tilde{\Gamma}^i$ in terms of the Christoffel symbols at any stage of the evolution.

B. Initial data

One main purpose of this paper is to provide a detailed comparison of binary-black-hole collisions obtained with different initial-data types. We now describe the different initial data available inside the code. Specifically, these are puncture, Misner, and superposed Kerr-Schild data.

The starting point for binary black-hole data of the puncture type is the Schwarzschild solution in isotropic coordinates, where the spacetime curvature is captured entirely within the conformal factor $\psi = e^{\phi} = (1 + \frac{m}{2r})$. In the case of time symmetry, these conformally flat data have been shown to generalize to an arbitrary number of black holes by merely adding the individual quotients in the conformal factor [64,65]

$$\psi = 1 + \sum_i \frac{m_i}{2|\vec{r} - \vec{r}_i|}, \tag{3}$$

where the index i labels the individual black holes. This time-symmetric initial configuration of multiple black holes is known as Brill-Lindquist data. As a further generalization of these data, spin and momentum can be incorporated in the form of a nonvanishing extrinsic curvature [66]. Finally, Brandt and Brügmann [20] have transformed this type of data into a form substantially more convenient for use in numerical simulations by applying a compactification to the internal asymptotically flat regions of the holes (see their paper for existence and uniqueness of the solutions for the Hamiltonian constraint). These data are commonly referred to as punctures and have been widely used in numerical simulations.

Inside the LEAN code, initial data of Brill-Lindquist type are implemented analytically using Eq. (3). More general classes of puncture data are made available via the TWOPUNCTURES thorn of Ansorg *et al.* [57], which solves the Hamiltonian constraint using spectral methods combined with transformations to a coordinate system specially adapted to the structure of the binary black-hole spacetime (see [57] for details).

The second class of initial data we study in this work is the axisymmetric Misner data [67] which represent a conformally flat spacetime containing two nonspinning equal-mass black holes at the moment of time symmetry ($K_{ij} = 0$). In Cartesian coordinates the three-metric γ_{ij} for this configuration can be written as

$$\gamma_{ij} = \psi_{\mathrm{M}}^4 \delta_{ij}, \tag{4}$$

where the conformal factor is given by

$$\psi_{\mathrm{M}} = 1 + \sum_n \frac{1}{\sinh n\mu}\left[\frac{1}{\sqrt{x^2 + y^2 + (z + z_n)^2}} + \frac{1}{\sqrt{x^2 + y^2 + (z - z_n)^2}}\right], \tag{5}$$

$$z_n = \coth n\mu, \tag{6}$$

and μ is a free parameter determining the initial separation of the holes D/M, where M is the ADM mass of the system.

As an alternative to these two conformally flat data types, the LEAN code allows the use of nonspinning black-hole binary data based on the Kerr-Schild solution for a single black hole [68,69]. The invariance of the structure of the Kerr-Schild data under boost transformations has motivated their use in boosted, superposed form. Even though these superposed data do not exactly satisfy the Einstein constraints for finite separation of the holes, they have been studied extensively in the literature, both as initial data and in the context of binary-black-hole evolutions (see, for example, [51,70–74]). Whenever we speak

of superposed Kerr-Schild data in the remainder of this work, we thus refer to this direct superposition of the data which has been used in evolutions before. We are currently not aware of any time evolutions presented in the literature that start with Kerr-Schild data *after* applying a constraint solving procedure.

In order to construct the data, we follow the approach of Ref. [51]. The solution of a single boosted, nonspinning Kerr-Schild hole with mass parameter m and velocity v^i is calculated according to the prescription presented in Appendix B. The two solutions thus obtained for black holes at positions ${}^{\mathrm{A}}x^i$ and ${}^{\mathrm{B}}x^i$ are then superposed according to

$$ {}^{\mathrm{KS}}\gamma_{ij} = {}^{\mathrm{A}}\gamma_{ij} + {}^{\mathrm{B}}\gamma_{ij} - \delta_{ij}, \tag{7} $$

$$ {}^{\mathrm{KS}}K^i_j = {}^{\mathrm{A}}K^i{}_j + {}^{\mathrm{B}}K^i{}_j, \tag{8} $$

$$ {}^{\mathrm{KS}}\beta_i = {}^{\mathrm{A}}\beta_i + {}^{\mathrm{B}}\beta_i, \tag{9} $$

$$ {}^{\mathrm{KS}}\alpha = ({}^{\mathrm{A}}\alpha^{-2} + {}^{\mathrm{B}}\alpha^{-2} - 1)^{-1/2}. \tag{10} $$

We note that, with this specific superposition, lapse α and shift β^i obey the close-limit condition, i.e. they lead to the lapse and shift of a single Kerr-Schild hole in the limit of zero separation.

C. Gauge conditions

An important ingredient in the recent success of numerical simulations of black-hole binaries has been the implementation of improved gauge conditions. In terms of the "3 + 1" decomposition, the coordinate invariance of general relativity is represented by the freedom to arbitrarily specify the lapse function α and the shift vector β^i. While the particular choice of these functions leaves unaffected the physical properties of the spacetime, it can have a dramatic effect on the stability properties of a numerical simulation.

In the past, the majority of gauge conditions have been designed with the purpose to drive the system of variables towards a stationary configuration (see e.g. [16,75,76]). In combination with the use of comoving coordinates, this approach led to the first simulation of a complete binary black-hole orbit [17]. More recent developments, however, have shown a tendency towards allowing the black holes to move across the computational domain (see e.g. [51,53] for single moving black holes and head-on collisions and [15,18,19,23] for orbiting black holes). We have implemented in the LEAN code both the use of algebraic gauge conditions along the lines reported in [53] and live-gauge conditions similar to those presented in [18,19] for the evolutions of black holes of the moving-puncture type (see also [77] for a more detailed numerical study and [78] for an analytic study of these types of gauge choices). Experimentally, we have found variations in these live-gauge conditions to manifest themselves most conspicuously in the profile of the variables $\tilde{\Gamma}^i$ near the punctures. In particular, we have noticed that steep gradients in these functions resulted in poor convergence properties of the merger time of the black holes or, worse, instabilities. We have found optimal performance of our code in this respect by evolving the gauge variables according to

$$ \partial_t \alpha = \beta^i \partial_i \alpha - 2\alpha K, \tag{11} $$

$$ \partial_t \beta^i = B^i, \tag{12} $$

$$ \partial_t B^i = \partial_t \tilde{\Gamma}^i - \eta B^i. \tag{13} $$

Initially we have experimented with setting $\eta = 2$, but observed an instability in the outermost refinement boundary for coarser resolutions. We have found the choice $\eta = 1$ to cure that instability while preserving the good convergence properties of the code and therefore use this value throughout this work. The gauge variables are initialized by using zero shift with a precollapsed lapse $\alpha = e^{-2\phi} = \sqrt{\chi}$.

The gauge conditions (11)–(13) not only provide stable evolutions, but also facilitate a comparatively simple method to track the black-hole position. As has been shown in Ref. [24] the vanishing of χ at the puncture in conjunction with Eq. (A6) implies that

$$ \frac{dx^i}{dt} = -\beta^i. \tag{14} $$

We have implemented this relation via interpolation of the shift vector at the puncture location and subsequent update of the position using a second-order Runge-Kutta method. In practice, we find excellent agreement between the resulting locations of the puncture and the coordinate center of the apparent horizon as calculated by AHFINDERDIRECT from surface integrals of the global coordinates over the horizon.

In the case of the evolutions of Kerr-Schild data, we have also experimented with these gauge conditions. So far, however, we have not managed to obtain long-term stable evolutions in this way. We have therefore reverted to the approach of using algebraic gauge according to the procedure described in [51]. That is, we prescribe analytic trajectories ${}^{\mathrm{A}}x^i(t)$, ${}^{\mathrm{B}}x^i(t)$ for black holes A and B and calculate the resulting gauge functions by superposing the analytic gauge of the individual holes. Following [53] we prescribe the analytic slicing condition in the form of the densitized lapse Q. We thus obtain

$$ {}^{\mathrm{KS}}\beta^i = {}^{\mathrm{KS}}\gamma^{ij}({}^{\mathrm{A}}\beta_j + {}^{\mathrm{B}}\beta_j), \tag{15} $$

$$ {}^{\mathrm{KS}}Q = {}^{\mathrm{KS}}\gamma^{-1/2}({}^{\mathrm{A}}\alpha^{-2} + {}^{\mathrm{B}}\alpha^{-2} - 1)^{-1/2}. \tag{16} $$

Here the quantities denoted with an A or a B are the analytic expressions for the individual black holes and

${}^{KS}\gamma_{ij}$ is the superposed metric defined in Eq. (7). In practice, we calculate the lapse from its densitized counterpart and the determinant of the numerical three-metric via $\alpha = \gamma_{\rm num}^{1/2} Q$. We emphasize that we use the densitized lapse only for algebraic slicing, but work with the unmodified lapse in all simulations using live-gauge conditions.

The trajectories used to evaluate the positions and velocities for the gauge functions associated with the individual black holes are obtained from fifth-order polynomials $x^i + v^i t + a^i t^2/2 + j^i t^3/6 + q^i t^4/24$ during the earlier stages of the infall of the black holes. In a time interval $t_1 < t < t_2$ we perform a smooth (up to the fourth derivative) transition of these polynomials to the static function $x^i = 0$. By virtue of the close-limit property of the superposed gauge (15) and (16), we thus obtain a smooth transition of the gauge to that of a single nonspinning Kerr-Schild hole.

The most difficult part in this procedure is to determine the coefficients v^i, a^i, j^i, q^i and t_1, t_2 so that one obtains a stable simulation. We have only managed to obtain stable evolutions using gauge trajectories that are close to the coordinate trajectories of the apparent horizon center, in particular, in the late stages of the infall. In practice, the black holes collide along the z axis and we set the x and y components of all coefficients to zero. The remaining z components are then obtained iteratively: The black holes are evolved with some initial guess for the coefficients (normally those used for the simulation with the next smaller initial separation). The apparent horizon center is tracked until this simulation becomes unstable and we adjust the parameters to make the gauge trajectory agree better with the horizon motion. This process is repeated until a stable simulation is obtained. Some minor variations of the parameters are possible while preserving the stability of the simulation but do not have a significant impact on the resulting waveforms, as is discussed below in Sec. IV B 2. The exact parameters used for the Kerr-Schild simulations in this work are given below in Table III. Unless specified otherwise, we use the trajectories labeled "a" in that table.

D. Black-hole excision

Evolutions of puncture-type initial data have been performed in the past both with and without the use of black-hole excision (see e. g. [16,17,21,48,75]). Those without excision have commonly been achieved by factoring out the irregular part of the conformal factor while evolving only the regular remainder. It is a remarkable and surprising feature of the moving-puncture evolutions introduced in [18,19] that these evolutions have been successful using neither excision nor the factoring out of the irregular part of the conformal factor. Below we will follow the same approach for our puncture/Brill-Lindquist and Misner evolutions.

In order to evolve Kerr-Schild data, however, we need to use black-hole excision. In contrast to puncture data, the spatial slices of the Kerr-Schild data do contain the physical singularity of the black hole at $r = 0$, which needs to be removed from the computational domain. Inside the LEAN code we have implemented black-hole excision using either one-sided derivatives or extrapolation techniques. So far, we have obtained better stability properties using extrapolation which is the method of choice for all simulations presented in this work. This particular excision algorithm has been described in detail in Refs. [51–53]. In the LEAN code the moving excision has now been generalized to work with moving refinement components. For this purpose each black hole has been assigned a particular refinement level it resides in (the finest level in all simulations presented in this work). Excision for this black hole is then only performed on this refinement level and communication to coarser levels is performed exclusively via the restriction procedure inside CARPET. Special care must be taken in the black-hole excision if the refinement component has been moved because the integer grid indices i, j, k no longer correspond to the same coordinate position x, y, z as on previous time steps. Because the set of excision boundary points is stored in terms of their indices i, j, k, rather than their coordinate positions, we must recalculate the list of excision boundary points every time the refinement component moves. This process does not involve changing any of the BSSN variables, however; it merely corrects the bookkeeping of the excision mask.

With a correct list of excision points available at every time step, we thus apply extrapolation of the BSSN variables via second-order polynomials during each iteration of the iterated Crank-Nicholson (ICN) cycle according to the procedure in Sec. 3 of Ref. [52]. After the completion of the whole time step, the code checks for the position of the black hole and adjusts the center of the excision region if necessary. As a minor modification compared with the excision method of the MAYA code used in [51–53], we use the horizon finder to track the black-hole motion and move the excision region accordingly.

So far, we have not succeeded in combining black-hole excision with the fourth-order discretization of the spatial derivatives. The problems largely arise from the need to use an excision boundary of thickness ≥ 2 to accommodate the wider fourth-order accurate stencils. For this reason, we use second-order discretization in space for all simulations using black-hole excision.

E. Mesh refinement

A further area of remarkable progress in numerical relativity in recent years is that of mesh refinement, which is used almost routinely now in various forms in black-hole simulations. The need for using mesh refinement, or essentially equivalent techniques based on specially adapted coordinates such as the "fish-eye transformation" [79],

arises from the presence of vastly different length scales in the spacetimes. On the one hand, a code has to resolve the steep gradients near the black-hole horizon, typically leading to length scales comparable with the mass of the hole. On the other hand, the typical wavelength associated with the ringing of a black hole is 1 order of magnitude larger. Furthermore, the calculation of accurate waveforms makes it necessary to extract waves at sufficiently large radii, ideally, in the wave zone. This requires the use of computational grids at least 2 orders of magnitude larger than the radius of a single black hole. With current computational power, this can only be achieved inside the framework of mesh refinement. Simulations of moving black holes add the extra requirement of dynamic or adaptive refinement.

In the LEAN code, mesh refinement is provided by the CARPET package. Dynamic refinement based on CARPET has already been reported in [80]. Here we use a refined version of this method. CARPET provides a routine which performs a *regridding* operation at regular intervals. That is, it interprets a steerable parameter string which contains the exact specifications of all refinement components in terms of their corner positions. Inside the LEAN code, we control this parameter string via a separate thorn REGRIDINFO which works as follows. This thorn creates a map between each refinement component and the black hole it is tied to (a zero entry meaning the component is not tied to black-hole motion and remains stationary). The black-hole motion, in turn, is monitored, either using the horizon finder or the puncture tracking method according to Eq. (14). The corner positions of the refinement components are adjusted according to the motion of the black holes. The REGRIDINFO thorn further performs checks on the internal consistency of the grid specifications and, if necessary, expands a component to guarantee that all finer components are accommodated with a minimum number of grid points between the refinement boundaries. Similarly, it expands components once the black-hole position comes too close to a refinement boundary.

Finally, the thorn allows for the merger of previously separate refinement components. This is triggered by the distance between two components decreasing below a user-specified threshold value. Again, the parameter string used by CARPET is updated accordingly and the regridding completes the dynamic adjustment of the mesh refinement. We find this technique to work very reliably and to preserve remarkably well the expected convergence properties of the code, as will be demonstrated below in Sec. III.

For a given simulation the initial grid consists of two types of cubic refinement levels, n outer levels centered on the origin which remain stationary throughout the simulation and m levels with two components centered around either black hole. In the remainder of this work we specify the exact setup by giving the resolution h on the finest level as well as the radius of the cubes excluding ghost zones required for interprocessor communication. The grid spacing always increases by a factor of 2 from one level to the next coarser refinement level. For example,

$$\{(256, 128, 74, 24, 12, 6) \times (1.5, 0.75), h = 1/48\}$$

specifies a grid with six fixed outer components of radius 256, 128, 74, 24, 12, and 6, respectively, and two refinement levels with two components each with radius 1.5 and 0.75 centered around either hole. The resolution is $h = 1/48$ on the finest level and successively increases to $8/3$ on the outermost level. In this work we will use equatorial as well as octant symmetry which reduces the number of points by a factor of 2 or 8, respectively. The grid setups used for the simulations of this work are summarized in Table I.

F. Discretization of the BSSN equations

In Appendix A we have listed explicitly the ϕ and χ version of the BSSN equations as used in the LEAN code. The discretization of the spatial derivatives has been implemented in the form of second-order as well as fourth-order accurate stencils. With the exception of the advection derivatives of the form $\beta^i \partial_i f$, these stencils are centered. Advection derivatives, on the other hand, are approximated with lopsided stencils

$$\partial_x f = \frac{1}{2dx}(-f_{i+2di,j,k} + 4f_{i+di,j,k} - 3f_{i,j,k}), \tag{17}$$

$$\partial_x f = \frac{1}{12dx}(f_{i+3di,j,k} - 6f_{i+2di,j,k} + 18f_{i+di,j,k} - 10f_{i,j,k} - 3f_{i-di,j,k}), \tag{18}$$

respectively, for second- and fourth-order accurate discre-

TABLE I. Grid setup and numerical schemes used for the simulations presented in this work. The resolutions used for the convergence studies are $h_1 = 1/48$, $h_2 = 1/44$, $h_3 = 1/40$ for models R1 and BL2, $h_1 = 1/28$, $h_2 = 1/24$, $h_3 = 1/20$ for model KS4, and $h_1 = 1/400$, $h_2 = 1/360$, $h_3 = 1/320$ for model M4.

Model	Scheme	Grid
R1	ICNχ_4	$\{(192, 128, 74, 24, 12, 6) \times (1.5, 0.75), h_i\}$
BL1	RKχ_4	$\{(256, 128, 96, 32, 16) \times (4, 2, 1), 1/48\}$
BL2	RKχ_4	$\{(256, 128, 96, 32, 16) \times (4, 2, 1), h_i\}$
BL3	RKχ_4	$\{(256, 128, 96, 32, 16) \times (4, 2, 1), 1/48\}$
BL4	RKχ_4	$\{(256, 128, 96, 32, 16) \times (4, 2, 1), 1/48\}$
ISCO	ICNϕ_4	$\{(256, 128, 88, 24, 12, 8) \times (2.4, 1.2, 0.6), 1/40\}$
KS1	ICNϕ_2	$\{256, 128, 96, 32, 16) \times (4, 2), 1/24\}$
KS2	ICNϕ_2	$\{256, 128, 96, 32, 16) \times (4, 2), 1/24\}$
KS3	ICNϕ_2	$\{256, 128, 96, 32, 16) \times (4, 2), 1/24\}$
KS4	ICNϕ_2	$\{256, 128, 96, 32, 16) \times (4, 2), h_i\}$
M1	ICNχ_4	$\{60, 30, \frac{45}{2}, \frac{15}{2}, \frac{15}{4}) \times (\frac{15}{16}, \frac{15}{32}, \frac{15}{64}), \frac{3}{512}\}$
M2	ICNχ_4	$\{48, 24, 18, 6, 3) \times (\frac{3}{4}, \frac{3}{8}, \frac{3}{16}), \frac{3}{640}$
M3	ICNχ_4	$\{40, 20, 15, 5, \frac{5}{2}) \times (\frac{5}{8}, \frac{5}{16}, \frac{5}{32}), \frac{1}{256}\}$
M4	ICNχ_4	$\{32, 16, 12.8, 4, 2) \times (\frac{1}{2}, \frac{1}{4}, \frac{1}{8}), h_i\}$

tization, with $di = \mathrm{sgn}(\beta^x)$ and likewise for the y and z direction.

Using these representations for the spatial derivatives, the partial differential equations for the BSSN variables are integrated in time using the method of lines. Here the time discretization is performed using either the second-order accurate ICN scheme with two iterations [81] or standard fourth-order RK integration. The exact numerical implementation of the BSSN equations is thus determined by three parameters, the time integration scheme, the ϕ or χ version, and the order of the spatial discretization. In the remainder of this work, these different choices are referred to as RKχ_4, ICNϕ_2, and so on. The discretizations used for the simulations in this work are summarized together with the grid setups in Table I.

The Berger-Oliger–type mesh refinement provided by CARPET requires communication between the refinement levels, the so-called prolongation and restriction operation (see e.g. [55]). For fourth (second)-order discretization of the spatial derivatives, we use sixth (fourth)-order accurate prolongation in space with a total of nine (three) or six (two) buffer zones, respectively, for the RK and ICN time discretization (cf. Sec. 2.3 of [55]). Prolongation in time is always performed using third-order accuracy. The necessary infrastructure required for higher order prolongation in time and, thus, genuine fourth-order accurate communication between the refinement levels is not available in the currently used implementation of the mesh refinement. The fourth-order convergence found for the simulations of puncture and Brill-Lindquist data below indicates that this does not represent a problem for the type of simulations under discussion in this work.

G. Wave extraction

We extract gravitational waves from our numerical simulations by calculating the Newman-Penrose scalar Ψ_4 using the electromagnetic decomposition of the Weyl tensor which is described in Appendix C. The spatial derivatives required in this calculation are obtained using either second or fourth-order accurate stencils chosen in accordance with the spatial discretization of the BSSN evolution equations. The calculation of Ψ_4 as well as the extraction of modes have been tested with the analytic expression calculated for the Teukolsky wave [82] for both the $\ell = 2$, $m = 0$ and $\ell = 2$, $m = 2$ waves (cf. also Ref. [83]). In both cases, the evolutions have been carried out using the ICNϕ_2 implementation of the BSSN equations and resulted in second-order convergence of the waveforms.

Once Ψ_4 has been calculated on a sphere of constant extraction radius, the radiated energy and momenta are obtained from Eqs. (22)–(24) in Ref. [84]. In practice, we perform these calculations in a post-processing operation using the output data of Ψ_4. There, we calculate both the total radiated energy as well as the energy radiated in the dominant modes, $\ell = 2$, $m = \pm 2$ for orbiting configurations and $\ell = 2$, $m = 0$ for the head-on collisions. For all head-on collisions we find the dominant mode to be responsible for $>99\%$ of the total radiated energy; for the inspiral the dominant modes account for about 98.5% of the total energy.

III. BINARY BLACK-HOLE ORBITS

Before we compare the head-on collisions of different data types, we demonstrate the code's capability to produce evolutions of orbiting black-hole binaries with convergent waveforms. For this purpose we consider model $R1$ of Table I of Ref. [19]. Here two black holes with mass parameter $m = 0.483$ start at coordinate positions $x = \pm 3.257$ with linear momentum parameter $P = \pm 0.133$ in the y direction.

We evolve this configuration with a setup as specified for model R1 in Table I using three different resolutions, $h_1 = 1/48$, $h_2 = 1/44$, and $h_3 = 1/40$. The simulations are performed using equatorial symmetry across the orbital xy plane.

The resulting real part of the $\ell = 2$, $m = 2$ mode of the Newman-Penrose scalar Ψ_4 extracted at $r = 60M$ is shown in Fig. 1 for all three resolutions. We first note that the waveforms show good agreement with the results obtained from similar simulations in the literature [27,35]. A factor 2 discrepancy with Fig. 2 of [27] results from a trivial rescaling depending on the choice of the eigenmode basis [cf. their Eq. (4)].

With regard to a convergence analysis, we first note that the error manifests itself in two forms, a phase shift and an amplitude difference. We therefore study the convergence both with and without applying a phase correction to align the global maxima of the curves. For the convergence analysis one commonly assumes that the discretization

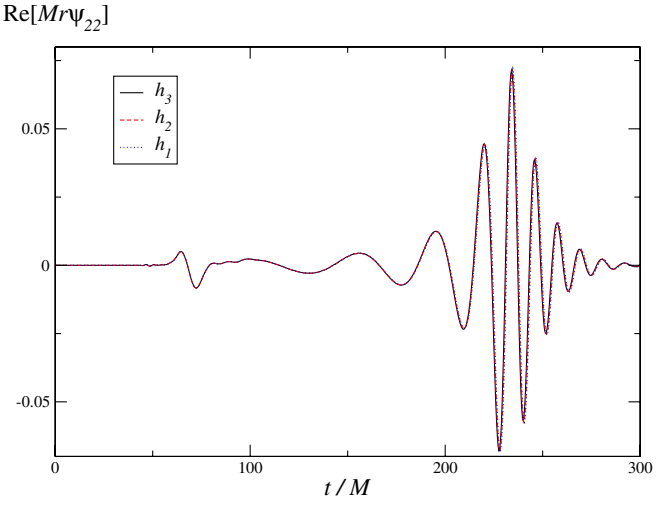

FIG. 1 (color online). The real part of the $\ell = 2$, $m = 2$ multipole of $Mr\Psi_4$ extracted from the $R1$ simulation at $r_{\mathrm{ex}} = 60M$ obtained for resolutions h_1, h_2, and h_3.

error be dominated by a leading order term $\mathcal{O}(h^\alpha)$, so that the numerical solution f_h of a given grid function is related to the continuum limit f by $f_h \approx f + Ch^\alpha$, where the coefficient C does not depend on the resolution h. Applying this relation to the three different resolutions h_1, h_2, h_3, one obtains

$$\frac{f_{h_3} - f_{h_2}}{f_{h_2} - f_{h_1}} \approx \frac{h_3^\alpha - h_2^\alpha}{h_2^\alpha - h_1^\alpha}. \tag{19}$$

Applied to our case, this relation leads to the value 1.58 for the case of fourth-order convergence. The convergence behavior of the $\ell = 2$, $m = 2$ multipole of $Mr\Psi_4$ with and without a phase correction is shown in Fig. 2, where we have amplified the differences between the higher resolution runs by the factor 1.58 expected for fourth-order convergence. The analysis shows good agreement with fourth-order convergence in both cases.

We similarly observe fourth-order convergence for the total radiated energy extracted at coordinate radii $r_{\rm ex} = 50M$, $60M$, and $70M$. We can use these results to estimate the uncertainties in the radiated energy resulting from finite resolution and extraction radii. The standard procedure to assess the impact of the resolution is to apply Richardson extrapolation, i.e. extrapolate the values obtained for a convergent simulation to the continuum limit $h \to 0$. Using this procedure we obtain $E_{\rm tot} = 3.558\%$, 3.543%, and 3.532%, respectively, of the total ADM mass M of the system at extraction radii $50M$, $60M$, and $70M$. This corresponds to an estimate of the discretization error in the radiated energy of about 1% for the high resolution $h_1 = 1/48$ and about 2% for the low resolution $h_3 = 1/40$.

In complete analogy to the procedure used to study the convergence with grid resolution h, we use these values to estimate the dependency of the radiated energy on the extraction radius. We find the resulting error to be modeled well by a $1/r_{\rm ex}$ falloff, i.e.

$$E_{\rm tot} \approx E_{\rm tot}|_{r_{\rm ex}=\infty} + \mathcal{O}\left(\frac{1}{r_{\rm ex}}\right). \tag{20}$$

Extrapolation of the results obtained at finite extraction radii thus gives a total radiated energy of $E_{\rm tot} = 3.466\%$ of the total ADM mass as well as an estimate for the error arising out of the use of a finite extraction radius of 2.7%, 2.3%, and 2.0%, respectively, for $r_{\rm ex} = 50M$, $60M$, and $70M$.

For the simulations presented in this work we universally find the errors due to finite differencing and finite extraction radius to point in opposite directions: finite resolution leads to underestimating the amount of radiated energy, and a finite extraction radius overestimates the energy. We therefore feel justified in using the sum of the individual errors as a conservative upper limit for the total error. In this case, we obtain a numerical error of 3% for the high resolution simulation using $r_{\rm ex} = 70M$.

Repeating the same calculation without including the artificial radiation burst due to the initial data,[2] we obtain a total radiated energy of $E_{\rm rad} = 3.408\%$ of the ADM mass. We note that this result for the energy shows excellent agreement with those presented in the literature (cf. Table III of [27]).

As a further test of the code we follow Ref. [18] and check the convergence properties of the Hamiltonian constraint on an equatorial axis shortly after the crossing of the punctures. The result is shown in Fig. 3 where we have amplified the high resolution result by a factor of 1.2^4 as expected for fourth-order convergence. In spite of the presence of some numerical noise, the figure demonstrates compatibility with overall fourth-order convergence of the simulations. We believe the larger amount of noise, as compared with the results of [18], to be a consequence of the use of mesh refinement and the discontinuous error terms at the refinement boundaries.

Unfortunately we are currently not able to obtain similar orbital simulations with Kerr-Schild data for want of suitable live-gauge conditions analogous to Eqs. (11)–(13). We therefore perform the comparison between these two data types and the Misner data inside the framework of head-on collisions.

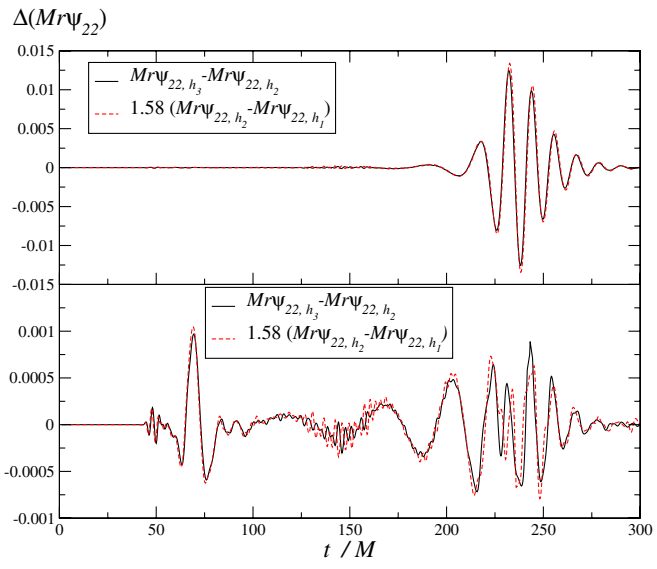

FIG. 2 (color online). Convergence analysis of the $\ell = 2$, $m = 2$ multipole of $Mr\Psi_4$ without correcting the phase error (upper panel) and after applying a phase correction (lower panel).

IV. HEAD-ON COLLISIONS

Head-on collisions represent the simplest form of black-hole binaries and have been studied numerically in various forms for a long time. The majority of such simulations has been performed using data of Misner [67] or Brill-Lindquist type (see e.g. [16,83,85–88]). As an alternative, collisions using Kerr-Schild data have been investigated in

[2] In practice, we ignore contributions at $t < r_{\rm ex} + 30M$ in the waveforms.

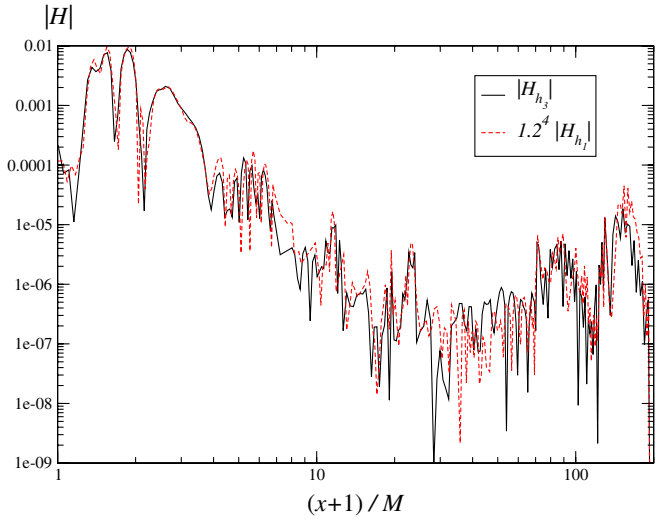

FIG. 3 (color online). Convergence analysis of the Hamiltonian constraint on the x axis at $t = 128M$, shortly after the crossing of the punctures.

[51]. Here we will study in detail head-on collisions of all three data types and compare the results.

The time evolutions of these two types of initial data present different difficulties and therefore require different evolution techniques. In summary, these are the use of second-order differencing, algebraic gauge conditions, and black-hole excision for the Kerr-Schild data, whereas Brill-Lindquist data are evolved using fourth-order discretization without using the black-hole excision procedure described in Sec. II D. As will be demonstrated below, we have obtained satisfactory convergence performance for the Kerr-Schild evolutions using the ϕ version of the BSSN equations. In the case of Brill-Lindquist data, we find the χ version more successful in providing fourth-order convergence. The Misner data are conceptually similar to Brill-Lindquist data. Experimentally, however, we have found the Misner data to lead to substantially larger amounts of numerical noise originating from the refinement boundaries when evolved in time with the Runge-Kutta method. Below we will show that the noise level is acceptable when using the second-order accurate ICN scheme instead.

In the notation of Sec. II F we therefore evolve the Kerr-Schild data using the ICNϕ_2 scheme, the Brill-Lindquist data with the[3] RKχ_4 and Misner data with the ICNχ_4 scheme. The resulting accuracy and convergence properties will be studied in detail in Sec. IV B.

A. Choice of initial parameters

A fundamental difficulty in the comparison between simulations of Brill-Lindquist, Kerr-Schild, and Misner data is the physical interpretation of the initial data sets. We first note that there exists no general method to rigorously quantify the degree to which two such initial configurations represent the same physical scenario. As an approximation, we determine the initial parameters as follows. First, we start the head-on collisions with two black holes of equal mass at rest, and thus eliminate the question of choosing initial linear momenta and mass ratios.

Except for a rescaling of the entire spacetime corresponding to a rescaling of the system's total mass, an initial configuration for a head-on collision of nonspinning, equal-mass black holes is characterized by one free parameter which can be viewed as a measure for the initial separation of the black holes or the binding energy of the system. In the case of Misner data, this degree of freedom is represented by the parameter μ in Eq. (5), whereas Brill-Lindquist and Kerr-Schild data require coordinate positions of the black holes so that the free parameter is the initial coordinate separation D. For the comparison of the different data types we fix the remaining free parameter by demanding that all three versions of the binary-black-hole spacetime have identical binding energy,

$$\frac{E_{\mathrm{b}}}{M} = 1 - \frac{M_1 + M_2}{M}, \tag{21}$$

where the irreducible black-hole masses M_1, M_2 are given by their respective apparent horizon masses. For illustration we plot in Fig. 4 the binding energy as a function of the coordinate distance D. For Misner data, the initial black-hole centers are approximated by their apparent horizon position which is ± 1.0 for all simulations discussed in this work.

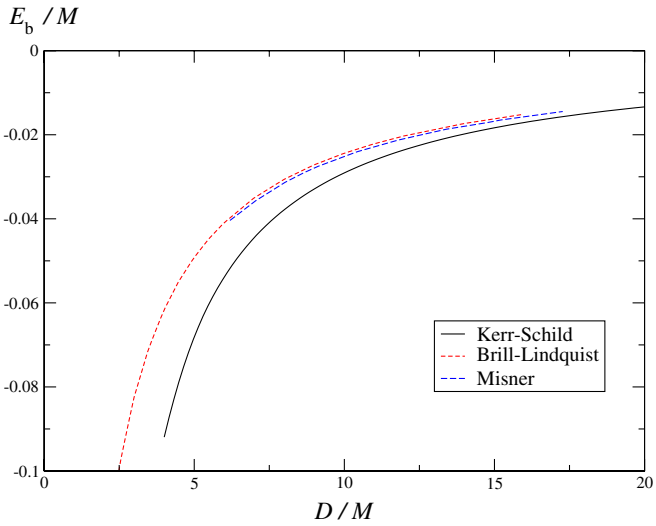

FIG. 4 (color online). Binding energy E_b/M for Kerr-Schild (solid line), Brill-Lindquist (short-dashed line), and Misner (long-dashed line) initial-data sets as a function of the coordinate distance D/M of the holes.

[3]With the exception of the simulations in Figs. 7 and 13 which are not used in this quantitative comparison.

The freedom in rescaling the spacetimes is fixed by demanding the total ADM mass to be unity for Kerr-Schild and Brill-Lindquist data which implies bare mass parameters $m_1 = m_2 = 0.5$ in both cases. In contrast, the conformal factor for the Misner data in Eq. (5) does not contain a bare mass parameter, and the ADM mass depends on the value of μ. Specifically, it decreases for larger μ and thus implies a larger black-hole separation D/M. In our simulations we have taken into account the different ADM masses of Kerr-Schild and Brill-Lindquist data on the one hand and Misner data on the other by using numerically higher resolutions for the Misner models. Relative to the ADM mass, however, the resolutions are rather similar to those used for Brill-Lindquist data. The exact ADM masses for all simulations discussed in this comparison are given in the third column of Table II.

Using this procedure, we have determined four different models with binding energies $E_b/M = -0.0290$, -0.0240, -0.0197, and -0.0169. These models are listed in Table II as BL1 − 4, KS1 − 4, and M1 − 4.

B. Testing the code

In this section we calibrate the performance of the code in the case of head-on collisions of all data types by performing convergence tests and investigating other error sources. For Brill-Lindquist data we also use results published in Ref. [83] starting from the approximate separation of the innermost stable circular orbit (ISCO).

1. Brill-Lindquist data

We assess the discretization error of the Brill-Lindquist simulations by evolving model BL2 of Table II using three different resolutions, $h_1 = 1/48$, $h_2 = 1/44$, and $h_3 = 1/40$, with a constant Courant factor of $dt/dx = 1/2$. We have studied the convergence of the resulting gravitational waveforms in complete analogy to the procedure used in Sec. III for black-hole inspiral. We observe fourth-order convergence as is demonstrated in Fig. 5 for the $\ell = 2$, $m = 0$ multipole extracted at $r_{ex} = 40M$. We similarly observe fourth-order convergence for the total radiated energy and use Richardson extrapolation to estimate the discretization error. We find the relative error at a resolution $h = 1/44$ to be less than 0.5% and use this value as a conservative upper limit.

In order to assess the impact of extracting waves at finite radii, we have studied the wave signal at extraction radii $40M$, $70M$, and $90M$. The resulting $\ell = 2$, $m = 0$ multipole of the Newman-Penrose scalar Ψ_4 is shown in the upper panel of Fig. 6. We estimate the uncertainty due to the extraction radius in the same way as in Sec. III and find the relative error in the total radiated energy to be of the order of 1% for $r_{ex} = 40M$ and less for the larger radii $70M$ and $90M$.

As a further test of our code, we compare the waveforms obtained for Brill-Lindquist data with those available in the literature. The head-on collisions presented commonly start with time-symmetric initial data of two holes at

TABLE II. Summary of the simulations performed in this work. Simulation R1 is the inspiral simulation described in Sec. III. The other simulations are the head-on collisions performed for the comparison of Brill-Lindquist, Misner, and superposed Kerr-Schild data. M is the total ADM mass of the spacetime, D the initial coordinate separation of the holes (for Misner data we list the parameter μ instead), and E_b the binding energy $M - M_1 - M_2$. E_{tot}, E_{ini}, and E_{rad} are the total radiated energy, the energy contained in the spurious initial burst, and the energy radiated in the inspiral and merger. The uncertainties included are those due to finite differencing, finite extraction radius, and the uncertainties in separating the merger signal from the spurious initial burst. For the Kerr-Schild data we also list the radiated energies obtained from extrapolation to $r_{ex} \to \infty$ with uncertainties due to finite differencing and the interference of the initial burst.

Model	D or μ	M	E_b/M	E_{tot}/M	E_{ini}/M	E_{rad}/M
R1	6.5	0.996	−0.0145	(3.466 ± 0.104)%	(0.058 ± 0.002)%	(3.408 ± 0.102)%
BL1	8.6	1	−0.0290	(0.0553 ± 0.0008)%	(0.0031 ± 0.0001)%	(0.0522 ± 0.0008)%
BL2	10.2	1	−0.0240	(0.0553 ± 0.0008)%	(0.0022 ± 0.0001)%	(0.0531 ± 0.0008)%
BL3	12.5	1	−0.0197	(0.0557 ± 0.0008)%	(0.0014 ± 0.0001)%	(0.0543 ± 0.0008)%
BL4	14.6	1	−0.0169	(0.0564 ± 0.0009)%	(0.0009 ± 0.0001)%	(0.0555 ± 0.0008)%
KS1	10.0	1	−0.0290	(0.1099 ± 0.0175)%	(0.0540 ± 0.0119)%	(0.0560 ± 0.0123)%
$r_{ex} \to \infty$				(0.0963 ± 0.0029)%	(0.0438 ± 0.0049)%	(0.0525 ± 0.0052)%
KS2	12.0	1	−0.0240	(0.0962 ± 0.0154)%	(0.0325 ± 0.0072)%	(0.0617 ± 0.0119)%
$r_{ex} \to \infty$				(0.0844 ± 0.0025)%	(0.0284 ± 0.0019)%	(0.0560 ± 0.0032)%
KS3	14.0	1	−0.0197	(0.0888 ± 0.0142)%	(0.0227 ± 0.0040)%	(0.0661 ± 0.0110)%
$r_{ex} \to \infty$				(0.0789 ± 0.0024)%	(0.0198 ± 0.0010)%	(0.0591 ± 0.0023)%
KS4	16.0	1	−0.0169	(0.0855 ± 0.0137)%	(0.0163 ± 0.0028)%	(0.0692 ± 0.0112)%
$r_{ex} \to \infty$				(0.0751 ± 0.0023)%	(0.0140 ± 0.0007)%	(0.0611 ± 0.0021)%
M1	3.573	0.231	−0.0290	(0.0555 ± 0.0017)%	(0.0031 ± 0.0001)%	(0.0524 ± (0.0016)%
M2	3.757	0.191	−0.0240	(0.0556 ± 0.0017)%	(0.0021 ± 0.0001)%	(0.0535 ± (0.0016)%
M3	3.948	0.157	−0.0197	(0.0560 ± 0.0017)%	(0.0014 ± 0.0001)%	(0.0546 ± (0.0017)%
M4	4.096	0.135	−0.0169	(0.0567 ± 0.0017)%	(0.0009 ± 0.0001)%	(0.0558 ± (0.0017)%

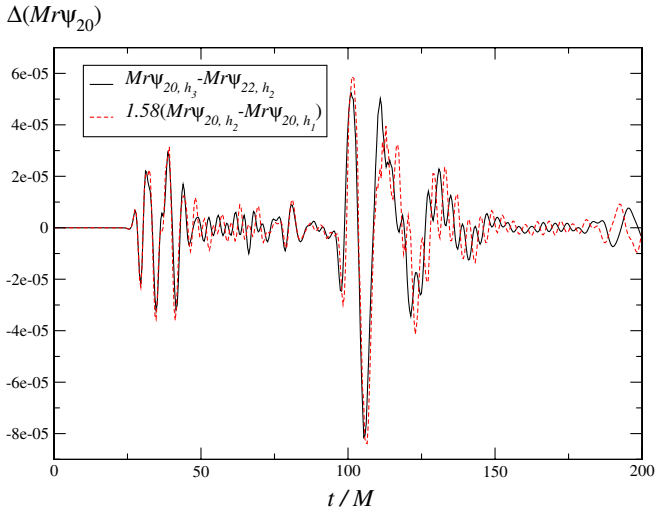

FIG. 5 (color online). Convergence analysis for the $\ell = 2$, $m = 0$ mode of the Newman-Penrose scalar Ψ_4 extracted at $r_{\rm ex} = 40M$. The difference between the runs with higher resolutions has been amplified by a factor 1.58 expected for fourth-order convergence.

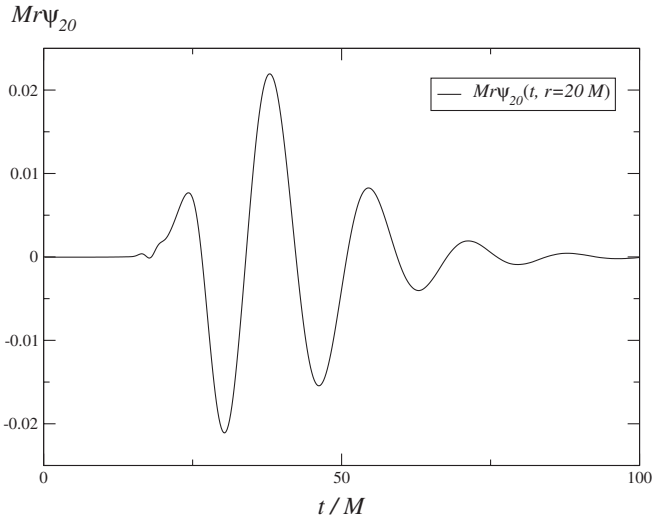

FIG. 7. The $\ell = 2$, $m = 0$ mode of $Mr\Psi_4$ extracted at $r_{\rm ex} = 20M$ from a head-on collision of Brill-Lindquist data starting from the approximate ISCO separation (cf. Fig. 5 in Ref. [83]).

positions $\pm 1.1515M$. This value has been calculated in Refs. [89,90] for the ISCO. The $\ell = 2$, $m = 0$ mode of the Newman-Penrose scalar Ψ_4 of this configuration has been calculated in [83] at an extraction radius $r_{\rm ex} = 20M$. In Fig. 7 we plot our result extracted at the same radius and obtained using the setup labeled "ISCO" in Table I. Up to the trivial rescaling factor of 2 mentioned above, we find excellent agreement with Fig. 5 in Ref. [83]. To our knowledge, similar results obtained with larger initial separations of the holes have not yet been published. It is part of the motivation of this work to provide such an extension of the existing work.

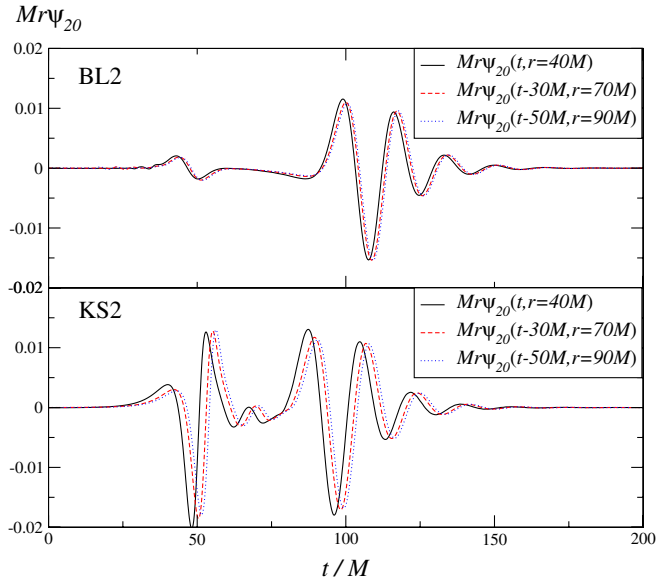

FIG. 6 (color online). The $\ell = 2$, $m = 0$ multipole obtained for models BL2 (upper panel) and KS2 (lower panel) extracted at $r_{\rm ex} = 40M$, $70M$, and $90M$.

We finally address one conceptual difference between the Brill-Lindquist and Misner data on the one side and Kerr-Schild data on the other. Whereas the former initial data are time symmetric, the superposed Kerr-Schild data do not satisfy this requirement, even for a vanishing velocity parameter. We thus cannot rule out that the individual Kerr-Schild holes do actually have a small boost and thus represent a slightly different physical configuration. Unfortunately, there exists no rigorous way to quantify the linear momenta of the individual holes in the Kerr-Schild spacetime, although the hypothesis of small momenta is compatible with the small nonzero initial coordinate velocities of the apparent horizon positions of $v = 0.05$ towards each other which we observe for the Kerr-Schild holes. For this reason we proceed differently and instead consider the impact of small initial boosts as an additional uncertainty in our study. We quantitatively study this effect using a modified version of model BL4. Specifically, we use puncture data, where initial linear momenta pointing towards each other are applied to the individual black holes in the form of nonzero Bowen-York [66] momentum parameters $P = 0.035$ and $P = 0.067$. All other parameters for these puncture models are kept at the values of model BL4.

In Fig. 8 we show the resulting waveforms at $r_{\rm ex} = 70M$ shifted in time to align their global extrema. The differences in the waveforms are rather small and we obtain for the energy radiated in the infall and merger $E_{\rm rad} = 0.05601 \pm 0.0008$ and 0.05795 ± 0.0009, respectively, of the ADM mass. Compared with the nonboosted result 0.0555 ± 0.0008, this corresponds to systematic deviations of about 1% and 4%.

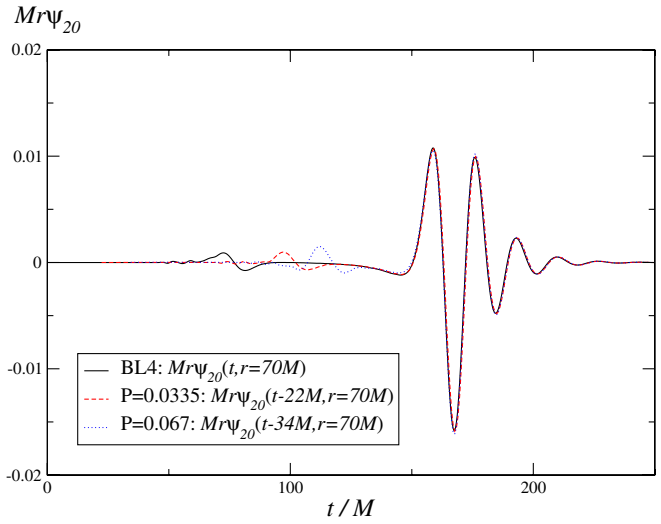

FIG. 8 (color online). The $\ell = 2$, $m = 0$ mode of $Mr\Psi_4$ extracted at $r_{\rm ex} = 70M$ for model BL4 (solid line), as well as puncture initial data with $P = \mp 0.0335$ (dashed line) and $P = \mp 0.067$ (dotted line) for the holes starting at coordinate positions $z = \pm 7.3$.

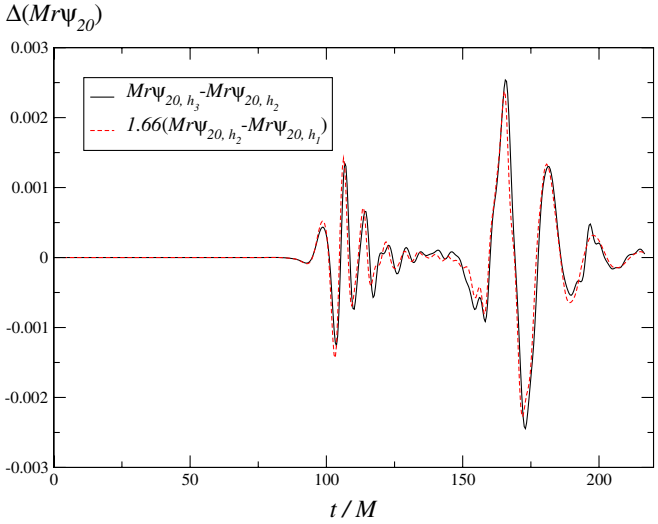

FIG. 9 (color online). Convergence analysis of the $\ell = 2$, $m = 0$ mode of Ψ_4 obtained at $r_{\rm ex} = 90M$ for model KS4 using resolutions $h_1 = 1/28$, $h_2 = 1/24$, and $h_3 = 1/20$. The differences between the high resolution results has been amplified by a factor of 1.66 expected for second-order convergence.

2. Kerr-Schild data

By evolving the Kerr-Schild models of Table II at different resolutions, we find model KS4 with the largest initial separation to exhibit the largest uncertainties. We therefore focus in our convergence analysis on this model to obtain conservative upper limits for the discretization error. We have evolved this model using the finest resolutions $h_1 = 1/28$, $h_2 = 1/24$, and $h_3 = 1/20$ and a constant Courant factor of $1/4$. Compared with the Brill-Lindquist data we have to use these seemingly coarser resolutions on the finest level because the coordinate radius of the apparent horizon is larger in the Kerr-Schild case and the use of excision prohibits the use of refinement components inside the apparent horizon. We emphasize, however, that relative to the coordinate radius of the horizon, about $r_{\rm ah} = 2M_{1,2}$ for Kerr-Schild data and $r_{\rm ah} = M_{1,2}/2$ for Brill-Lindquist data, our setup results in a finer resolution in the Kerr-Schild case.

The resulting differences in the $\ell = 2$, $m = 0$ multipole of the Newman-Penrose scalar are shown in Fig. 9 and demonstrate second-order convergence. Using Richardson extrapolation as before, we obtain an error of 3% in the radiated energy due to the discretization of the Einstein equations.

In comparison with the Brill-Lindquist data, we observe larger differences in the amplitude of the gravitational waves extracted at different radii. This is shown in the lower panel of Fig. 6 where we plot the $\ell = 2$, $m = 0$ multipole obtained for model KS2 at $r_{\rm ex} = 40M, 70M$, and $90M$. Systematically investigating the total radiated energy for all Kerr-Schild simulations, we find the results compatible with a $1/r_{\rm ex}$ falloff as in Sec. III. For example, the energies extracted from model KS4 at $40M$, $70M$, and $90M$ using a resolution $h = 1/24$ are 0.0984%, 0.884%, and 0.855% of the total mass M, respectively. Extrapolation to infinite radius results in 0.0752% of the mass and a relative error of 13% at extraction radius $r_{\rm ex} = 90M$. We find the uncertainties due to the extraction radius to be very similar for all other Kerr-Schild simulations and to be essentially independent of the grid resolution.

In view of this large uncertainty we will always present in the remainder of this work two values for the energies resulting from simulations of Kerr-Schild data. The numerical values obtained at the largest extraction radius $r_{\rm ex} = 90M$, together with uncertainties due to extraction radius, discretization, and interference of the initial pulse, and the value extrapolated to infinite radius with uncertainties due to discretization and the initial pulse, are listed in Table II.

A further difficulty in the case of the Kerr-Schild data arises from the relatively large amount of spurious radiation due to the initial data. This spurious radiation manifests itself as a pulse in the waveform starting at $t \approx r_{\rm ex}$. In the two panels of Fig. 6, for example, the initial burst leads to local extrema in the waveforms near $t \approx 50M$. The amplitude of the pulse is, however, substantially larger for the Kerr-Schild (lower panel) than the Brill-Lindquist (upper panel) data. For the smaller separations used in our analysis, it becomes nontrivial to disentangle this pulse from the actual merger signal, and it is not entirely clear how much radiated energy is due to the black-hole merger and how much is due to the spurious pulse. We attempt to bracket these uncertainties by using a variable threshold $t_{\rm thresh}$ so that radiation at $t < t_{\rm thresh}$ is considered part of the initial pulse and radiation at larger t part of the merger

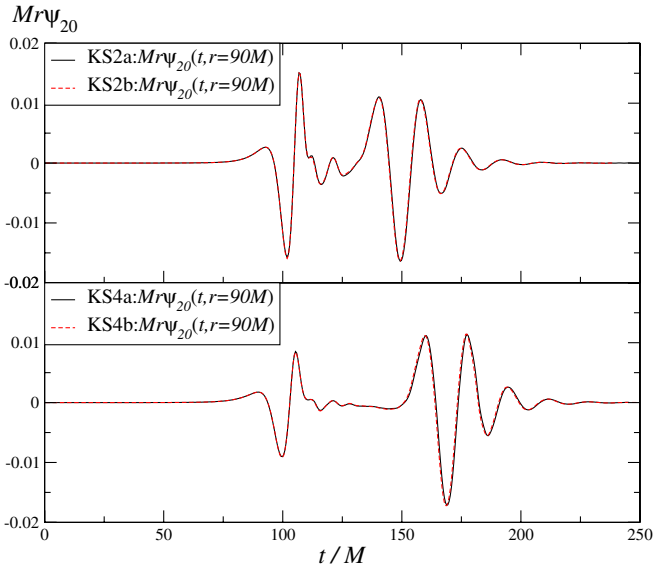

FIG. 10 (color online). The $\ell = 2$, $m = 0$ multipole of $Mr\Psi_4$ extracted at $r_{\rm ex} = 90M$ for model KS2 (upper panel) and KS4 (lower panel) using gauge trajectories labeled in Table III as "a" (solid curve) and "b" (dashed curve).

signal. At a given extraction radius we then vary $t_{\rm thresh}$ in the range $r_{\rm ex} + 30M$ to $r_{\rm ex} + 40M$. The two resulting energy contributions are given by their average values obtained over this interval plus or minus an error given by the upper and lower bounds.

We finally discuss the impact of the gauge trajectories on the resulting waveforms. We have already mentioned in Sec. II C that the gauge trajectories need to closely resemble the motion of the center of the apparent horizon and are obtained iteratively by approximating the horizon trajectory. For this comparison we have constructed gauge trajectories according to this procedure, first, by fixing v^z to be zero[4] and, second, by also adjusting this parameter in the iterative procedure. The parameters for the trajectories are listed in Table III, and in Fig. 10 we show as examples the resulting waveforms extracted at $r_{\rm ex} = 90M$ for simulations KS2a, b (upper panel) and KS4a, b (lower panel) obtained using a resolution $h = 1/24$. The resulting waveforms are practically indistinguishable, and the differences in the energies for the initial pulse, the merger signal, and the total waveform are about 1% and thus significantly smaller than the uncertainties due to the finite differencing and the extraction radius. The same applies to variations from 2/3 to zero in the evolution parameter σ in Eq. (A5).

3. Misner data

Finally, we estimate the numerical error of the evolutions starting from Misner data. All evolutions of these data using the Runge-Kutta time integration have resulted in significant contaminations of the resulting waveforms by numerical noise. A comprehensive analysis of the performance of different numerical schemes in evolutions of Misner data and the underlying causes is beyond the scope of this work, but we will show here that sufficiently accurate simulations can be obtained by using the ICN scheme instead of Runge-Kutta and also choosing a small Courant factor of 1/8.

[4]This velocity parameter is not to be confused with that used in the calculation of the initial data for γ_{ij} and K_{ij} which is always zero.

TABLE III. Parameters for the gauge trajectories used for the Kerr-Schild simulations.

Model	z/M	v^z	$a^z M$	$j^z M^2$	$q^z M^3$	$\frac{t_1}{M}$	$\frac{t_2}{M}$
KS1 a	± 5	0	∓ 0.037	± 0.0038	0	10	35
KS1 b	± 5	∓ 0.08	∓ 0.0061	∓ 0.0002	0	20	40
KS2 a	± 6	0	∓ 0.029	± 0.004	∓ 0.000278	25	50
KS2 b	± 6	∓ 0.06	∓ 0.008	± 0.0004	∓ 0.00002	20	44
KS3 a	± 7	0	∓ 0.022	± 0.0027	∓ 0.000165	25	57
KS3 b	± 7	∓ 0.04	∓ 0.007	± 0.0003	∓ 0.000012	25	57
KS4 a	± 8	0	∓ 0.018	± 0.002	± 0.000104	34.5	84.7
KS4 b	± 8	∓ 0.03	∓ 0.006	± 0.00027	∓ 0.000012	50	70

The resulting differences in the $\ell = 2$, $m = 0$ mode of $Mr\Psi_4$ obtained for model M4 are shown in Fig. 11. Compared with the Brill-Lindquist and Kerr-Schild evolutions, we observe larger amounts of high frequency noise in the early stages of the simulations due to the spurious initial radiation. Still, the overall behavior is compatible with the expected second-order convergence. Using the same methods as before, we find the resulting uncertainty in the radiated energy due to finite differencing to be of the order of 1%. With regard to the extraction radius, we find Misner data to behave similarly to Brill-Lindquist data.

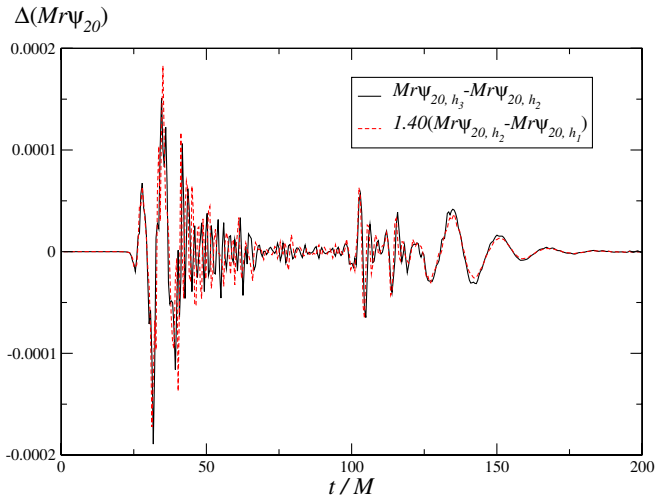

FIG. 11 (color online). Convergence analysis of the $\ell = 2$, $m = 0$ mode of Ψ_4 obtained for model M4 using resolutions $h_1 = 1/400$, $h_2 = 1/360$, and $h_3 = 1/320$. The differences between the high resolution results has been amplified by a factor of 1.40 expected for second-order convergence.

The resulting uncertainty due to the use of finite radii is about 2% at $r_{ex} = 40M$ and 1% at $70M$ or $90M$.

C. Results

In order to compare the different initial-data types, we have evolved all models listed in Table II with the grid setups described in Table I. We summarize the results in Fig. 12 which shows the $\ell = 2$, $m = 0$ modes obtained at extraction radius $r_{ex} = 90M$, and in Table II where we list the initial parameters and the total radiated energy E_{tot} as well as the contributions of the spurious initial pulse E_{ini} and the merger signal E_{rad}. The radiated energies have been extracted at $r_{ex} = 90M$, and for Kerr-Schild data we also give the extrapolated values for $r_{ex} \to \infty$. The uncertainties are those obtained in the previous section. In the case of Kerr-Schild data starting from small separations, the error for E_{ini} and E_{rad} is amplified significantly by the uncertainties in separating the initial pulse from the merger signal.

In Fig. 12 we note the substantially larger amount of artificial radiation due to the initial data in the Kerr-Schild case (dashed curve). Second, we observe excellent agreement between the waveforms obtained from Misner and Brill-Lindquist data (the solid and long-dashed curves are practically indistinguishable) and good qualitative agreement with the Kerr-Schild results. There remains, however, a small systematic deviation to the effect that the Kerr-Schild waves have a 5%–10% larger amplitude. We have already seen, however, that the finite extraction radius results in an overestimation of the wave amplitudes, in particular, in the Kerr-Schild case.

In order to quantify this effect, we consider the radiated energies in Table II. We first note that within the uncertainties Brill-Lindquist and Misner data result in identical amounts of energy in the initial-data pulse, the merger waveform as well as the total radiation. In contrast, the total radiated energy obtained from the Kerr-Schild data is significantly larger than that of Misner and Brill-Lindquist simulations. This excess energy is largely due to the spurious initial pulse, however, and for models KS1 and KS2, the energy contained in the physically important merger waveform agrees within the error bounds with its Misner and Brill-Lindquist counterparts. In particular, this is true for the values obtained from extrapolation to infinite extraction radius. The situation becomes more complicated, however, for the Kerr-Schild models starting from larger separations, in particular, for model KS4. With the error estimates obtained in the previous section, we obtain a lower limit of $E_{rad} = 0.0580\%$ of the ADM mass which exceeds the upper limit of simulation BL4 of $E_{rad} = 0.0563$ by about 3%. While we have taken into account in the derivation of these results the errors arising from finite differencing and the wave extraction at finite radius, it is possible that systematic errors are responsible for the remaining discrepancy. We have seen in Sec. IV B 1 that small boosts give rise to radiated energies a few percent larger than those obtained for initially time-symmetric data. A further systematic error results from the constraint violations inherent to the superposed Kerr-Schild data. Unfortunately there exists, to our knowledge, no literature on time evolutions of the constraint-solved version of the Kerr-Schild data. Filling this gap is beyond the scope of this paper as it requires the addition of elliptic solvers, currently not available in the LEAN code. It is therefore currently not possible to rigorously quantify the impact of the constraint violations on the resulting waveforms. We note, however, that the amount of spurious initial gravitational radiation inherent to the superposed Kerr-Schild data is significantly larger than the discrepancies we observe. If this spurious initial radiation is a signature of the constraint violations, it is certainly possible that the discrepancies

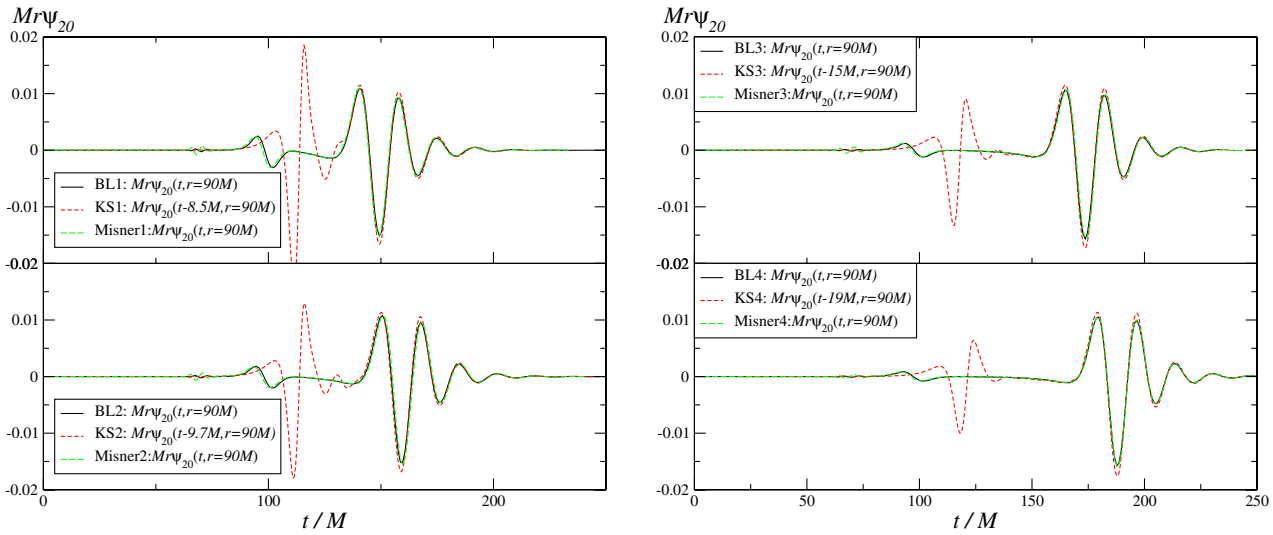

FIG. 12 (color online). The $\ell = 2$, $m = 0$ mode of $Mr\Psi_4$ at $r_{ex} = 90M$ for the Brill-Lindquist, Kerr-Schild, and Misner versions of models 1–4. For presentation purposes, the Kerr-Schild data have been shifted in time to align the maxima of the waveforms.

observed here are due to the constraint violations of the Kerr-Schild data.

A further interesting question is the dependence of the radiated energies on the initial black-hole separations. We have already noticed that the amount of spurious initial radiation decreases at larger separations as is expected. Correspondingly, we observe the expected increase in the energy radiated in the infall and merger at larger initial separations. This increase is relatively weak, though, for the cases studied here, especially for Brill-Lindquist and Misner data. It would be desirable to probe a larger range of initial distances, in particular, smaller separations, to study this behavior in more detail. Unfortunately, such an extension encounters difficulties at either end of the spectrum.

In the case of Kerr-Schild data, separations smaller than that of KS1 lead to a severe contamination of the actual signal by the spurious wave content and thus do not allow a physically meaningful interpretation. At the upper end, we are limited by the construction of suitable gauge trajectories. The prolonged infall puts stronger demands on the fine-tuning of the gauge trajectories. So far, we have not managed to obtain stable evolutions starting from Kerr-Schild data with $D > 16M$.

In the case of Brill-Lindquist data, we do not encounter such difficulties with the gauge because of the universality of the live-gauge conditions (11)–(13). Results starting from small separations, however, are subject to the difficulties due to the initial wave burst. This is illustrated by evolving a set of Brill-Lindquist data starting with initial separations $D_{\rm BL} = 2.3M$, $4.3M$, and $6.3M$. The resulting waveforms as obtained with the setup labeled ISCO in Table I are shown together with that of model BL1 in Fig. 13. We clearly notice a substantial contamination of the waveforms at small separations by radiation inherent to the initial data. In consequence, an accurate calculation of the gravitational wave energy generated in the head-on collision becomes highly nontrivial even for Brill-Lindquist data. For this reason the comparison performed in this study is currently limited to the window of binding energies or separations covered by the results in Table II.

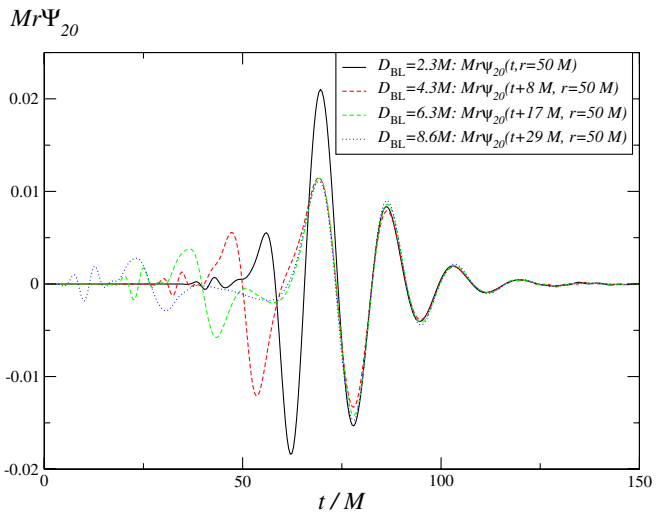

FIG. 13 (color online). Waveforms obtained from Brill-Lindquist data starting at various initial separations. The data have been shifted in time to align the maxima of the waveforms.

V. SUMMARY AND CONCLUSIONS

In this work, we have presented in detail a numerical code designed for the simulation of black-hole binaries in the framework of three-dimensional, nonlinear general relativity. The code facilitates black-hole evolutions using different initial-data types and evolution techniques.

It has been demonstrated that the code is capable of evolving state-of-the-art binary-black-hole orbits using the recently developed moving-puncture technique. With regard to the accuracy of the results, we find it crucial to use a fourth-order discretization of the spatial derivatives appearing in the BSSN formulation of the Einstein field equations. The resulting simulations yield convergent waveforms which agree well with results presented in the literature. The same holds for the radiated energy which we estimate to be $3.408\% \pm 0.102\%$ of the total ADM mass. The code is thus suitable for detailed studies of various types of multiple black-hole simulation with regard to the generation of accurate waveform templates.

In preparation for the comparison of black-hole collisions using different types of initial data, we test the code's performance and estimate in detail the error margins associated with the different evolutions. Specifically, we separately demonstrate convergence of the code for simulations starting from Brill-Lindquist, superposed Kerr-Schild, and Misner data. We also study in depth the dependence of the resulting waveforms on the extraction radii. While the resulting uncertainties are relatively small for Brill-Lindquist and Misner data, we find the use of finite extraction radii to be the dominant error source for simulations of Kerr-Schild data. In the case of Brill-Lindquist data we further demonstrate the code's reliability by comparing head-on collisions with results available in the literature.

We use the code to provide a detailed comparison of black-hole-binary head-on collisions using all three data types. In addition to the total mass of the system, either initial configuration has one free parameter which is specified by fixing the binding energy $E_{\rm b}/M$ of the system. We have compared the resulting waveforms for four initial configurations.

The resulting waveforms obtained from Brill-Lindquist and Misner data show excellent agreement and predicts an energy radiated in the infall and merger of about 0.052%–0.056% of the total ADM mass M with the exact value increasing with the initial black-hole separation. In parallel, the amount of energy due to spurious radiation inherent to the conformally flat initial data decreases from

$0.0031\%M$ to $0.0009\%M$ as the initial separation of the holes is increased from a binding energy $E_b = -0.029M$ to $-0.0169M$. The uncertainties in these results for both data types are of the order of a few percent. While this good agreement might be expected, given the similar nature of the two data types, it is reassuring to confirm this expectation with high accuracy using current numerical techniques.

In the case of the superposed Kerr-Schild data, we observe a substantially larger amount of energy in the spurious gravitational radiation due to the initial data, about a factor 15 larger than for the other data types. For sufficiently large separations, most of this spurious wave content radiates away before the merger of the holes and can thus be distinguished from the actual signal of the merger and ring-down. For the smaller separations studied, however, this distinction becomes more difficult and leads to a non-negligible uncertainty in the amount of energy radiated in the infall and merger of the holes.

In comparison with the conformally flat data types, the merger waveforms extracted at finite radius show larger amplitudes in the case of the Kerr-Schild simulations by 5%–10%. The agreement of the resulting radiated energies in the infall and merger becomes much better, though, after extrapolating results to infinite extraction radius. Still, for large black-hole separations there remains a discrepancy of a few % in the merger energy between Kerr-Schild data on the one side and Brill-Lindquist and Misner data on the other, even when taking into account remaining uncertainties in the simulations. We can therefore not rule out systematic errors affecting the accuracy of the Kerr-Schild simulations.

Such systematic errors can arise from the fact that the initial data are not inherently time symmetric and might imply small initial boosts of the individual holes. By evolving puncture data with nonvanishing Bowen-York momentum, we have shown that small boosts can account for the discrepancies of the observed magnitude. A second systematic error arises from the constraint violations of the Kerr-Schild data. In particular, we observe the energy contained in the spurious initial radiation, likely to be a signature of the constraint violations, to be significantly larger than the differences we observe.

Finally, we mention future directions of research encouraged by this study. First, it will be valuable to understand the origin for the relatively large uncertainties in the wave amplitudes obtained from Kerr-Schild data at finite extraction radius or, conversely, why wave extraction appears to work remarkably well for the Misner and puncture simulations at radii significantly smaller than the wave zone. Second, it will be important to produce evolutions of the constraint-solved version of the Kerr-Schild data and compare the results with those of the present study. An important question in this regard also concerns the amount of spurious initial radiation. A key advantage of Kerr-Schild–type initial data over conformally flat data is the fact that they contain the Kerr solution as a limit. They are therefore particularly promising candidates for producing initial-data sets containing black holes with very large spins with minimal artificial radiation (see, for example, [91] for a discussion of artificial radiation in black-hole spacetimes with large spins). It is thus important to study how the solving of the constraints reduces the large amounts of artificial radiation observed here in the nonspinning case.

ACKNOWLEDGMENTS

I thank Marcus Ansorg, Erik Schnetter, and Jonathan Thornburg for providing the TWOPUNCTURE thorn, CARPET, and AHFINDERDIRECT. I further thank Bernd Brügmann, Jose Gonzalez, Mark Hannam, Sascha Husa, and Christian Königsdörffer for illuminating discussions in all areas of this work. I also thank Bernard Kelly, Pablo Laguna, Ken Smith, Deirdre Shoemaker, and Carlos Sopuerta for fruitful discussions concerning all aspects of the Kerr-Schild evolutions. This work was supported by the DFG Grant No. SFB/Transregio 7 "Gravitational Wave Astronomy," and computer time allocations at HLRS Stuttgart and LRZ Munich. I acknowledge support from the ILIAS Sixth Framework programme.

APPENDIX A: THE BSSN EVOLUTION EQUATIONS

The BSSN equations are implemented in the LEAN code using either the set of variables defined in Eq. (1) or the variable χ in place of ϕ as defined in Eq. (2). The ϕ version of the BSSN equations used in LEAN is given by

$$\partial_t \tilde{\gamma}_{ij} = \beta^m \partial_m \tilde{\gamma}_{ij} + 2\tilde{\gamma}_{m(i}\partial_{j)}\beta^m - \tfrac{2}{3}\tilde{\gamma}_{ij}\partial_m \beta^m - 2\alpha\tilde{A}_{ij}, \tag{A1}$$

$$\partial_t \phi = \beta^m \partial_m \phi + \tfrac{1}{6}(\partial_m \beta^m - \alpha K), \tag{A2}$$

$$\begin{aligned}\partial_t \tilde{A}_{ij} = {} & \beta^m \partial_m \tilde{A}_{ij} + 2\tilde{A}_{m(i}\partial_{j)}\beta^m - \tfrac{2}{3}\tilde{A}_{ij}\partial_m \beta^m \\ & + e^{-4\phi}(\alpha R_{ij} - D_i D_j \alpha)^{\mathrm{TF}} \\ & + \alpha(K\tilde{A}_{ij} - 2\tilde{A}_i{}^m \tilde{A}_{mj}),\end{aligned} \tag{A3}$$

$$\partial_t K = \beta^m \partial_m K - D^m D_m \alpha + \alpha(\tilde{A}^{mn}\tilde{A}_{mn} + \tfrac{1}{3}K^2), \tag{A4}$$

$$\begin{aligned}\partial_t \tilde{\Gamma}^i = {} & \beta^m \partial_m \tilde{\Gamma}^i - \tilde{\Gamma}^m \partial_m \beta^i + \tfrac{2}{3}\tilde{\Gamma}^i \partial_m \beta^m + 2\alpha\tilde{\Gamma}^i_{mn}\tilde{A}^{mn} \\ & + \tfrac{1}{3}\tilde{\gamma}^{im}\partial_m \partial_n \beta^n + \tilde{\gamma}^{mn}\partial_m \partial_n \beta^i - \tfrac{4}{3}\alpha\tilde{\gamma}^{im}\partial_m K \\ & + 2\tilde{A}^{im}(6\alpha\partial_m \phi - \partial_m \alpha) \\ & - (\sigma + \tfrac{2}{3})(\tilde{\Gamma}^i - \tilde{\gamma}^{mn}\tilde{\Gamma}^i_{mn})\partial_k \beta^k.\end{aligned} \tag{A5}$$

Here D_i is the covariant derivative operator and R_{ij} the Ricci tensor associated with the physical three-metric γ_{ij}, and the superscript TF denotes the trace-free part. We also note that the last term in the evolution equation (A5)

vanishes in the continuum limit by virtue of the definition of $\tilde{\Gamma}^i$ in Eq. (1). With the addition of this term we follow Yo *et al.* [92] who introduced this modification to improve the stability of the BSSN formulation in cases of relaxed symmetry assumptions of the spacetime under study. We set the free parameter σ in this term to $2/3$.

The χ version of the evolution system is obtained by substituting $\chi = e^{-4\phi}$. The evolution equations for the variables χ, $\tilde{A}^{ij}$, and $\tilde{\Gamma}^i$ are then given by

$$\partial_t \chi = \beta^m \partial_m \chi + \tfrac{2}{3}(\alpha K - \partial_m \beta^m), \tag{A6}$$

$$\begin{aligned}\partial_t \tilde{A}_{ij} = {} & \beta^m \partial_m \tilde{A}_{ij} + 2\tilde{A}_{m(i}\partial_{j)}\beta^m - \tfrac{2}{3}\tilde{A}_{ij}\partial_m \beta^m \\ & + \chi(\alpha R_{ij} - D_i D_j \alpha)^{\mathrm{TF}} \\ & + \alpha(K\tilde{A}_{ij} - 2\tilde{A}_i{}^m \tilde{A}_{mj}),\end{aligned} \tag{A7}$$

$$\begin{aligned}\partial_t \tilde{\Gamma}^i = {} & \beta^m \partial_m \tilde{\Gamma}^i - \tilde{\Gamma}^m \partial_m \beta^i + \tfrac{2}{3}\tilde{\Gamma}^i \partial_m \beta^m + 2\alpha \tilde{\Gamma}^i_{mn}\tilde{A}^{mn} \\ & + \tfrac{1}{3}\tilde{\gamma}^{im}\partial_m \partial_n \beta^n + \tilde{\gamma}^{mn}\partial_m \partial_n \beta^i - \frac{4}{3}\alpha \tilde{\gamma}^{im}\partial_m K \\ & - \tilde{A}^{im}\left(3\alpha \frac{\partial_m \chi}{\chi} + 2\partial_m \alpha\right) \\ & - \left(\sigma + \frac{2}{3}\right)(\tilde{\Gamma}^i - \tilde{\gamma}^{mn}\tilde{\Gamma}^i_{mn})\partial_k \beta^k,\end{aligned} \tag{A8}$$

while Eqs. (A1) and (A4) remain valid without modification.

APPENDIX B: THE ADM VARIABLES OF A SINGLE BOOSTED KERR-SCHILD BLACK HOLE

The purpose of this section is to calculate the ADM functions γ_{ij}, K_{ij}, α, and β^i as functions of the laboratory coordinates x^μ for a nonspinning boosted black hole with mass parameter m in Kerr-Schild coordinates moving with speed v^i in the laboratory rest frame.[5] The rest frame coordinates of the black hole are related to the laboratory coordinates by a Lorentz transformation,

$$x^{\bar{\alpha}} = \Lambda^{\bar{\alpha}}{}_{\mu} x^{\mu}, \tag{B1}$$

where the transformation matrix is given by

$$\Lambda^{\bar{\alpha}}{}_{\mu} = \begin{pmatrix} \gamma & -\gamma v_m \\ -\gamma v^a & \delta^a{}_m + (\gamma - 1)\frac{v^a v_m}{\vec{v}^2} \end{pmatrix}. \tag{B2}$$

In the black-hole rest frame, the spacetime metric is given by (see e.g. [72])

$$g_{\bar{\alpha}\bar{\beta}} = \eta_{\bar{\alpha}\bar{\beta}} + 2H\ell_{\bar{\alpha}}\ell_{\bar{\beta}}, \tag{B3}$$

where

$$H = \frac{m}{\bar{r}}, \tag{B4}$$

$$\ell_{\bar{\alpha}} = \left[1, \frac{x_{\bar{a}}}{\bar{r}}\right], \tag{B5}$$

$$\bar{r} = x^{\bar{a}} x_{\bar{a}}, \tag{B6}$$

and indices of $x^{\bar{a}}$ and $v^{\bar{a}}$ are raised and lowered with the flat space metric $\delta_{\bar{a}\bar{b}}$.

The spacetime metric in the laboratory frame is obtained from that in the black-hole frame by a Lorentz transformation,

$$g_{\mu\nu} = \Lambda^{\bar{\alpha}}{}_{\mu}\Lambda^{\bar{\beta}}{}_{\nu} g_{\bar{\alpha}\bar{\beta}} = \eta_{\mu\nu} + 2H\ell_\mu \ell_\nu, \tag{B7}$$

where we have used the fact that H and ℓ_μ behave like a scalar and vector, respectively, and the Minkowski metric is invariant under Lorentz transformations.

From the spacetime metric we directly obtain the three-metric, its inverse, as well as lapse and shift,

$$\gamma_{mn} = \delta_{mn} + 2H\ell_m \ell_n, \tag{B8}$$

$$\gamma^{mn} = \delta^{mn} - 2H\delta^{mk}\delta^{nl}\ell_k \ell_l/[1 + 2H(\ell_0)^2], \tag{B9}$$

$$\alpha = [1 + 2H(\ell_0)^2]^{-1/2}, \tag{B10}$$

$$\beta_m = 2H\ell_0 \ell_m, \tag{B11}$$

$$\beta^m = 2H\ell_0 \delta^{mk}\ell_k/[1 + 2H(\ell_0)^2]. \tag{B12}$$

The extrinsic curvature is obtained from the derivatives of the three-metric according to

$$\begin{aligned}K_{mn} &= -\frac{1}{2\alpha}(\partial_t \gamma_{mn} - \mathcal{L}_\beta \gamma_{mn}) \\ &= -\frac{1}{2\alpha}(\partial_t \gamma_{mn} - 2D_{(m}\beta_{n)}),\end{aligned} \tag{B13}$$

where $\mathcal{L}_\beta$ denotes the Lie derivative along the shift vector and D_m the three-dimensional covariant derivative operator.

The derivatives of the three-metric are most conveniently expressed in terms of H and ℓ_m,

$$\partial_t \gamma_{mn} = 2(\ell_m \ell_n \partial_t H + H\ell_n \partial_t \ell_m + H\ell_m \partial_t \ell_n), \tag{B14}$$

$$\begin{aligned}D_{(m}\beta_{n)} = {} & 2[\ell_0 \ell_{(m}\partial_{n)}H + H\ell_{(m}\partial_{n)}\ell_0 + H\ell_0 \partial_{(m}\ell_{n)}] \\ & - \Gamma^k_{mn}\beta_k.\end{aligned} \tag{B15}$$

Finally, the derivatives of H and ℓ_μ are given by

$$\partial_\mu H = -\Lambda^{\bar{\alpha}}{}_{\mu}\frac{m x^{\bar{\alpha}}}{\bar{r}^3}, \tag{B16}$$

$$\partial_\mu \ell_\nu = \Lambda^{\bar{a}}{}_{\mu}\Lambda^{\bar{b}}{}_{\nu}\delta_{\bar{a}\bar{b}}\frac{1}{\bar{r}} - \Lambda^{\bar{a}}{}_{\mu}\Lambda^{\bar{b}}{}_{\nu}\frac{x_{\bar{a}}x_{\bar{b}}}{\bar{r}^3}. \tag{B17}$$

In summary, the function for calculating the ADM variables of a boosted black hole in Kerr-Schild coordinates at a particular point requires as input the coordinates of the

[5] See, for example, [93] for a discussion of the superposition of Kerr-Schild holes with nonvanishing spin.

point in the laboratory frame as well as the velocity $\vec{v}$ of the hole. First, the coordinates are transformed into the rest frame of the black hole according to Eq. (B1). Next H and $\ell_{\bar{\alpha}}$ follow from Eqs. (B4) and (B5) and give the spacetime metric components (B7). The three-metric, lapse, and shift follow from Eqs. (B8), (B10), and (B12). Together with the extrinsic curvature (B13), these are returned to the calling function as the ADM variables of the boosted Kerr-Schild metric.

APPENDIX C: THE ELECTROMAGNETIC DECOMPOSITION OF THE WEYL TENSOR AND WAVE EXTRACTION

We calculate the Newman-Penrose scalar Ψ_4 from the Weyl tensor via

$$\Psi_4 = C_{\alpha\beta\gamma\delta} n^\alpha \bar{m}^\beta n^\gamma \bar{m}^\delta, \tag{C1}$$

where n and $\bar{m}$ form part of a null-tetrad ℓ, n, m, $\bar{m}$ such that all their inner products vanish except

$$-\ell \cdot n = 1 = m \cdot \bar{m} \tag{C2}$$

Specifically, we construct ℓ, n, and m from the orthonormal triad vectors u, v, and w according to

$$\begin{aligned} \ell^\alpha &= \frac{1}{\sqrt{2}}(\hat{n}^\alpha + u^\alpha), \qquad n^\alpha = \frac{1}{\sqrt{2}}(\hat{n}^\alpha - u^\alpha), \\ m^\alpha &= \frac{1}{\sqrt{2}}(v^\alpha + i w^\alpha), \end{aligned} \tag{C3}$$

where $\hat{n}^\mu$ is the timelike orthonormal vector. The triad u, v, w is constructed via Gram-Schmidt orthonormalization starting with

$$\begin{aligned} u^i &= [x, y, z], \qquad v^i = [xz, yz, -x^2 - y^2], \\ w^i &= \epsilon^i{}_{mn} v^m w^n, \end{aligned} \tag{C4}$$

where ϵ^{imn} represents the three-dimensional Levi-Civita tensor.

In the decomposition of the Weyl tensor we follow the presentation of Friedrich [94]. The electric and magnetic parts of the gravitational field are given by

$$E_{\alpha\beta} = \perp^\mu{}_\alpha \perp^\nu{}_\beta C_{\mu\rho\nu\sigma} n^\rho n^\sigma, \tag{C5}$$

$$B_{\alpha\beta} = \perp^\mu{}_\alpha \perp^\nu{}_\beta {}^*C_{\mu\rho\nu\sigma}, \tag{C6}$$

where $\perp^\mu{}_\alpha = \delta^\mu{}_\alpha + \hat{n}^\mu \hat{n}_\alpha$ is the projector onto the spacelike hypersurface and the $*$ denotes the Hodge dual. By virtue of the Gauss-Codazzi equations (see e.g. [95]), one can express the electromagnetic parts in terms of "3 + 1" variables according to

$$\begin{aligned} E_{ij} &= R_{ij} - \gamma^{mn}(K_{ij}K_{mn} - K_{im}K_{jn}), \\ B_{ij} &= \gamma_{ik}\epsilon^{kmn} D_m K_{nj}. \end{aligned} \tag{C7}$$

The Weyl tensor is then given in terms of the electric and magnetic parts by Eq. (3.10) of Ref. [94]. Inserting this relation together with Eqs. (C3) and (C7) into the definition (C1) enables us to express Ψ_4 exclusively in terms of "3 + 1" quantities

$$\begin{aligned} \Psi_4 = \frac{1}{2}[E_{mn}(v^m v^n - w^m w^n) - B_{mn}(v^m w^n + w^m v^n)] \\ - \frac{i}{2}[E_{mn}(v^m w^n - w^m v^n) + B_{mn}(w^m w^n + v^m v^n)]. \end{aligned}$$

In practice, Ψ_4 is calculated using this relation on the entire Cartesian grid and then interpolated onto coordinate spheres of different extraction radii. We then apply a mode decomposition using spherical harmonics $Y^{-2}_{\ell m}$ of spin-weight -2 [cf. Eq. (42) in Ref. [96]] according to

$$\Psi_4(t, \theta, \phi) = \sum_{\ell,m} \psi_{\ell m}(t) Y^{-2}_{\ell m}(\theta, \phi), \tag{C8}$$

$$\psi_{\ell m}(t) = \int \Psi_4(t, \theta, \phi) \overline{Y^{-2}_{\ell m}}(\theta, \phi) d\Omega. \tag{C9}$$

In this context we note that Ψ_4 is always extracted onto the entire coordinate sphere $\theta = 0 \ldots \pi$, $\phi = 0 \ldots 2\pi$, even when underlying symmetry of the physical problem is used to reduce the computational domain to a bitant or octant. In those cases we use the fact that the real part of Ψ_4 behaves like a scalar while the imaginary part of Ψ_4 behaves like a pseudoscalar, i.e. reverses its sign across symmetry boundaries.

APPENDIX D: PERFORMANCE OF THE CODE

The majority of simulations presented in this work have been performed using a 24 node Linux cluster. Each node contains four AMD 2200 GHz processors and provides 8 Gb of memory. Parallelization is implemented using the MPICH version 1.2.6 2004/08/08 libraries. The code has been compiled with version 4.0.2 2005091 of the gcc, g++, and gfortran compilers. Compared with alternative architectures (cf. Ref. [97]), we have noticed that this

TABLE IV. Performance summary for representative simulations presented in this work.

Simulation	dt/dx	#CPU	Memory (Gb)	Speed (M/CPUh)
R1 ($h = 1/40$)	1/2	12	20.1	0.620
R1 ($h = 1/44$)	1/2	16	26.4	0.347
R1 ($h = 1/48$)	1/2	24	35.2	0.225
BL4 ($h = 1/40$)	1/2	8	9.9	0.854
BL4 ($h = 1/44$)	1/2	12	12.5	0.582
BL4 ($h = 1/48$)	1/2	16	18.2	0.350
KS4 ($h = 1/20$)	1/4	8	8.1	0.571
KS4 ($h = 1/24$)	1/4	8	14.0	0.315
KS4 ($h = 1/28$)	1/4	16	22.5	0.171
M4 ($h = 1/320$)	1/8	8	9.1	0.269
M4 ($h = 1/360$)	1/8	12	12.3	0.162
M4 ($h = 1/400$)	1/8	12	17.5	0.111

architecture requires about 25% more memory resources for identical simulations.

In Table IV we summarize the performance of the code for simulations R1, BL4, KS4, and M4 of Table II using this architecture. The columns show the Courant factor dt/dx which scales linearly with the code's speed, the number of processors used in the simulation, the required memory, as well as the speed. The latter is measured in physical time in units of the ADM mass M of the system per real time and processor.

Regarding the memory usage, we observe minor variations, typically below 5%, in the course of the simulation. This is due to the merger of refinement components as the black holes approach each other. The merger of refinement components also leads to an increase in speed because the costly regridding operation is no longer required and the total number of grid points of the merged refinement component is smaller than the sum of the two individual ones prior to merging. All reported speeds are averages over the entire simulation.

[1] B. Abbott *et al.*, Phys. Rev. D **73**, 062001 (2006).
[2] B. Abbott *et al.*, Nucl. Instrum. Methods Phys. Res., Sect. A **517**, 154 (2004).
[3] F. Acernese *et al.*, Classical Quantum Gravity **22**, S869 (2005).
[4] M. Ando *et al.*, Classical Quantum Gravity **22**, S881 (2005).
[5] M. Hewitson *et al.*, Classical Quantum Gravity **22**, S891 (2005).
[6] L. Blanchet, Living Rev. Relativity **2006**, 4 (2006), http://www.livingreviews.org/Articles/lrr-2006-4/download/index.html.
[7] L. Blanchet, T. Damour, B. R. Iyer, C. M. Will, and A. G. Wiseman, Phys. Rev. Lett. **74**, 3515 (1995).
[8] L. Blanchet, T. Damour, and B. R. Iyer, Phys. Rev. D **51**, 5360 (1995); **54**, 1860(E) (1996).
[9] L. Blanchet, B. R. Iyer, C. M. Will, and A. G. Wiseman, Classical Quantum Gravity **13**, 575 (1996).
[10] T. Damour, A. Gopakumar, and B. R. Iyer, Phys. Rev. D **70**, 064028 (2004).
[11] C. Königsdörffer and A. Gopakumar, Phys. Rev. D **73**, 124012 (2006).
[12] T. W. Baumgarte and S. L. Shapiro, Phys. Rev. D **59**, 024007 (1998).
[13] M. Shibata and T. Nakamura, Phys. Rev. D **52**, 5428 (1995).
[14] Y. Bruhat, in *Gravitation: An Introduction to Current Research*, edited by L. Witten (Wiley, New York, 1962).
[15] F. Pretorius, Classical Quantum Gravity **22**, 425 (2005).
[16] M. Alcubierre, B. Brügmann, P. Diener, M. Koppitz, D. Pollney, E. Seidel, and R. Takahashi, Phys. Rev. D **67**, 084023 (2003).
[17] B. Brügmann, W. Tichy, and N. Jansen, Phys. Rev. Lett. **92**, 211101 (2004).
[18] M. Campanelli, C. O. Lousto, and Y. Zlochower, Phys. Rev. D **73**, 061501(R) (2006).
[19] J. G. Baker, J. Centrella, D.-I. Choi, M. Koppitz, and J. van Meter, Phys. Rev. D **73**, 104002 (2006).
[20] S. Brandt and B. Brügmann, Phys. Rev. Lett. **78**, 3606 (1997).
[21] P. Diener, F. Herrmann, D. Pollney, E. Schnetter, E. Seidel, R. Takahashi, J. Thornburg, and J. Ventrella, Phys. Rev. Lett. **96**, 121101 (2006).
[22] F. Pretorius, Phys. Rev. Lett. **95**, 121101 (2005).
[23] F. Pretorius, Classical Quantum Gravity **23**, S529 (2006).
[24] M. Campanelli, C. O. Lousto, P. Marronetti, and Y. Zlochower, Phys. Rev. Lett. **96**, 111101 (2006).
[25] J. G. Baker, J. Centrella, D.-I. Choi, M. Koppitz, and J. van Meter, Phys. Rev. Lett. **96**, 111102 (2006).
[26] F. Herrmann, I. Hinder, D. Shoemaker, and P. Laguna, Classical Quantum Gravity **24**, S33 (2007).
[27] J. G. Baker, J. Centrella, D.-I. Choi, M. Koppitz, J. van Meter, and M. C. Miller, Astrophys. J. **653**, L93 (2006).
[28] J. A. González, U. Sperhake, B. Brügmann, M. D. Hannam, and S. Husa, Phys. Rev. Lett. **98**, 091101 (2007).
[29] F. Herrmann, I. Hinder, D. Shoemaker, P. Laguna, and R. Matzner, arXiv:gr-qc/0701143.
[30] M. Campanelli, C. O. Lousto, Y. Zlochower, and D. Merritt, Astrophys. J. **659**, L5 (2007).
[31] M. Koppitz, D. Pollney, C. Reissweg, L. Rezzolla, J. Thornburg, P. Diener, and E. Schnetter, Phys. Rev. Lett. **99**, 041102 (2007).
[32] J. A. González, M. D. Hannam, U. Sperhake, B. Brügmann, and S. Husa, Phys. Rev. Lett. **98**, 231101 (2007).
[33] W. Tichy and P. Marronetti, arXiv:gr-qc/0703075 [Phys. Rev. D (to be published)].
[34] F. Herrmann, I. Hinder, D. M. Shoemaker, P. Laguna, and R. A. Matzner, arXiv:0706.2541.
[35] M. Campanelli, C. O. Lousto, and Y. Zlochower, Phys. Rev. D **74**, 041501 (2006).
[36] M. Campanelli, C. O. Lousto, Y. Zlochower, and D. Merritt Astrophys. J. **659**, L5 (2007).
[37] A. Buonanno, G. B. Cook, and F. Pretorius, Phys. Rev. D **75**, 124018 (2007).
[38] J. G. Baker, J. R. van Meter, S. T. McWilliams, J. Centrella, and B. J. Kelly, arXiv:gr-qc/0612024.
[39] E. Berti, V. Cardos, J. A. González, U. Sperhake, M. D. Hannam, S. Husa, and B. Brügmann, arXiv:gr-qc/0703053 [Phys. Rev. D (to be published)].
[40] H. P. Pfeiffer, D. A. Brown, L. E. Kidder, L. Lindblom, G. Lovelace, and M. Scheel, Classical Quantum Gravity **24**, S59 (2007).
[41] S. Husa, M. Hannam, J. A. González, U. Sperhake, and B. Brügmann, arXiv:0706.0904.
[42] M. D. Hannam, S. Husa, U. Sperhake, B. Brügmann, and J. A. González, arXiv:0706.1305.
[43] M. Shibata, K. Taniguchi, and K. Uryū, Phys. Rev. D **68**,

084020 (2003).
[44] P. Marronetti, M. D. Duez, S. L. Shapiro, and T. Baumgarte, Phys. Rev. Lett. **92**, 141101 (2004).
[45] M. Miller, P. Gressman, and W.-M. Suen, Phys. Rev. D **69**, 064026 (2004).
[46] M. Anderson, E. W. Hirschmann, L. Lehner, S. L. Liebling, P. M. Motl, D. Neilsen, C. Palenzuela, and J. E. Tohline, arXiv:0708.2720.
[47] M. D. Duez, Y. T. Liu, S. L. Shapiro, M. Shibata, and B. C. Stephens, Phys. Rev. D **73**, 104015 (2006).
[48] M. Alcubierre, B. Brügmann, P. Diener, F. Herrmann, D. Pollney, E. Seidel, and R. Takahashi, arXiv:gr-qc/0411137.
[49] J. Baker, M. Campanelli, C. O. Lousto, and R. Takahashi, Phys. Rev. D **65**, 124012 (2002).
[50] J. G. Baker, M. Campanelli, F. Pretorius, and Y. Zlochower, Classical Quantum Gravity **24**, S25 (2007).
[51] U. Sperhake, B. Kelly, P. Laguna, K. L. Smith, and E. Schnetter, Phys. Rev. D **71**, 124042 (2005).
[52] D. Shoemaker, K. Smith, U. Sperhake, P. Laguna, E. Schnetter, and D. Fiske, Classical Quantum Gravity **20**, 3729 (2003).
[53] U. Sperhake, K. L. Smith, B. Kelly, P. Laguna, and D. Shoemaker, Phys. Rev. D **69**, 024012 (2004).
[54] Cactus Computational Toolkit homepage, http://www.cactuscode.org/.
[55] E. Schnetter, S. H. Hawley, and I. Hawke, Classical Quantum Gravity **21**, 1465 (2004).
[56] Carpet Code homepage, http://www.carpetcode.org/.
[57] M. Ansorg, B. Brügmann, and W. Tichy, Phys. Rev. D **70**, 064011 (2004).
[58] J. Thornburg, Phys. Rev. D **54**, 4899 (1996).
[59] J. Thornburg, Classical Quantum Gravity **21**, 743 (2004); AIP Conf. Proc. 686, 247 (2003).
[60] R. Arnowitt, S. Deser, and C. W. Misner, in *Gravitation an Introduction to Current Research*, edited by L. Witten (John Wiley, New York, 1962), pp. 227–265.
[61] J. W. York, Jr., in *Sources of Gravitational Radiation*, edited by L. Smarr (Cambridge University Press, Cambridge, 1979), pp. 83–126.
[62] G. Nagy, O. E. Ortiz, and O. A. Reula, Phys. Rev. D **70**, 044012 (2004).
[63] G. Yoneda and H.-A. Shinkai, Phys. Rev. D **66**, 124003 (2002).
[64] C. Misner and J. Wheeler, Ann. Phys. (N.Y.) **2**, 525 (1957).
[65] D. R. Brill and R. W. Lindquist, Phys. Rev. **131**, 471 (1963).
[66] J. M. Bowen and J. W. York, Jr., Phys. Rev. D **21**, 2047 (1980).
[67] C. W. Misner, Phys. Rev. **118**, 1110 (1960).
[68] R. P. Kerr, Phys. Rev. Lett. **11**, 237 (1963).
[69] R. P. Kerr and A. Schild, in Proceedings of Symposia in Applied Mathematics Vol. XVII (1965), pp. 199–209.
[70] E. Bonning, P. Marronetti, D. Neilsen, and R. A. Matzner, Phys. Rev. D **68**, 044019 (2003).
[71] P. Marronetti, M. Huq, P. Laguna, L. Lehner, R. Matzner, and D. Shoemaker, Phys. Rev. D **62**, 024017 (2000).
[72] R. A. Matzner, M. F. Huq, and D. Shoemaker, Phys. Rev. D **59**, 024015 (1998).
[73] S. Brandt, R. Correll, R. Gómez, M. Huq, P. Laguna, L. Lehner, P. Marronetti, R. A. Matzner, D. Neilsen, and J. Pullin *et al.*, Phys. Rev. Lett. **85**, 5496 (2000).
[74] P. Marronetti and R. A. Matzner, Phys. Rev. Lett. **85**, 5500 (2000).
[75] M. Alcubierre and B. Brügmann, Phys. Rev. D **63**, 104006 (2001).
[76] M. Alcubierre, A. Corichi, J. González, D. Núñez, and M. Salgado, Classical Quantum Gravity **20**, 3951 (2003).
[77] J. R. van Meter, J. G. Baker, M. Koppitz, and D.-I. Choi, Phys. Rev. D **73**, 124011 (2006).
[78] C. Gundlach and J. M. Martin-Garcia, Phys. Rev. D **74**, 024016 (2006).
[79] J. Baker, M. Campanelli, and C. O. Lousto, Phys. Rev. D **65**, 044001 (2002).
[80] C. F. Sopuerta, U. Sperhake, and P. Laguna, Classical Quantum Gravity **23**, S579 (2006).
[81] S. A. Teukolsky, Phys. Rev. D **61**, 087501 (2000).
[82] S. A. Teukolsky, Phys. Rev. D **26**, 745 (1982).
[83] D. R. Fiske, J. G. Baker, J. R. van Meter, D.-I. Choi, and J. M. Centrella, Phys. Rev. D **71**, 104036 (2005).
[84] M. Campanelli and C. O. Lousto, Phys. Rev. D **59**, 124022 (1999).
[85] L. Smarr, A. Čadež, B. DeWitt, and K. Eppley, Phys. Rev. D **14**, 2443 (1976).
[86] P. Anninos, D. Hobill, E. Seidel, L. Smarr, and W.-M. Suen, Phys. Rev. Lett. **71**, 2851 (1993).
[87] P. Anninos, D. Hobill, E. Seidel, L. Smarr, and W.-M. Suen, Phys. Rev. D **52**, 2044 (1995).
[88] Y. Zlochower, J. G. Baker, M. Campanelli, and C. O. Lousto, Phys. Rev. D **72**, 024021 (2005).
[89] G. B. Cook, Phys. Rev. D **50**, 5025 (1994).
[90] T. W. Baumgarte, Phys. Rev. D **62**, 024018 (2000).
[91] M. D. Hannam, S. Husa, B. Brügmann, J. A. González, and U. Sperhake, Classical Quantum Gravity **24**, S15 (2007).
[92] H.-J. Yo, T. W. Baumgarte, and S. L. Shapiro, Phys. Rev. D **66**, 084026 (2002).
[93] C. Moreno, D. Nuñez, and O. Sarbach, Classical Quantum Gravity **19**, 6059 (2002).
[94] H. Friedrich, Classical Quantum Gravity **13**, 1451 (1996).
[95] E. Gourgoulhon, arXiv:gr-qc/0703035.
[96] B. Brügmann, M. González, M. D. Hannam, S. Husa, U. Sperhake, and W. Tichy, arXiv:gr-qc/0610128.
[97] P. Marronetti, W. Tichy, B. Brügmann, J. A. González, M. D. Hannam, S. Husa, and U. Sperhake, Classical Quantum Gravity **24**, S43 (2007).